Thesis for the degree of Licentiate of Engineering

Making predictions using χEFT

Boris D. Carlsson

Department of Fundamental Physics
Chalmers University of Technology
Gothenburg, Sweden 2015

Making predictions using χEFT
Boris D. Carlsson

Department of Fundamental Physics
Chalmers University of Technology
SE-412 96 Gothenburg
Sweden
Telephone +46 (0)31-772 1000

Cover:
χ^2 surface for the optimization of a leading-order nucleon-nucleon interaction from chiral effective field theory. At this order the theory depends only on two parameters – $\tilde{C}_{^1S_0}$ on the x-axis and $\tilde{C}_{^3S_1}$ on the y-axis. Two minima are shown, with the lower one being the global minimum. See Sec. 5.2.

Chalmers Reproservice
Gothenburg, Sweden 2015

Making predictions using χEFT

Boris D. Carlsson
Department of Fundamental Physics
Chalmers University of Technology

Abstract

In this thesis we explore the merits of chiral effective field theory (χEFT) as a model for low-energy nuclear physics. χEFT is an effective field theory based on quantum chromo dynamics (QCD) describing low-energy interactions of nucleons and pions. We estimate the inherent uncertainties of χEFT and the accompanying methods used to compute observables in order to test the predictive power of the model. We use experimental pion-nucleon, nucleon-nucleon and few-nucleon data to perform a simultaneous fit of the low-energy constants in χEFT. This results in small statistical uncertainties in the model. The results show a clear order-by-order improvement of χEFT with the systematical model error dominating the total error budget.

Keywords: nuclear physics, χEFT, uncertainty quantification, NN scattering, few-nucleon physics

This thesis is based on work from the following two papers. In the main text these papers will be referred to as Paper 1 and Paper 2, respectively.

Paper 1:
Statistical uncertainties of a chiral interaction at next-to-next-to leading order
A. Ekström, B. D. Carlsson, K. A. Wendt, C. Forssén, M. Hjorth-Jensen, R. Machleidt and S. M. Wild
J. Phys. G: Nucl. Part. Phys. 42 034003 (2015),
e-Print: arXiv:1406.6895

In this paper we constructed an N2LO χEFT potential where the LECs were fitted to nucleon-nucleon scattering data. We then performed a statistical analysis to obtain uncertainties for the LECs. These uncertainties were propagated to other observables such as deuteron properties.

Paper 2:
Uncertainty analysis and order-by-order optimization of chiral nuclear interactions
B. D. Carlsson, A. Ekström, C. Forssén, D. Fahlin Strömberg, O. Lilja, M. Lindby, B. A. Mattsson and K. A. Wendt
Submitted to Physical Review X, e-Print: arXiv:1506.02466

In this paper we improved upon the results presented in Paper 1. We constructed LO, NLO and N2LO potentials using a simultaneous fit to pion-nucleon, nucleon-nucleon and few-nucleon experimental data. We also included an estimate of the inherent model uncertainty, which improved the fitting procedure and allowed us to include more data. We performed a subsequent statistical analysis where we propagated statistical errors to selected bound-state properties in nuclei such as ^{4}He and ^{16}O.

In addition, the author has been involved in the work leading to the following publications. These works are **not** included in this thesis.

Effects of Three-Nucleon Forces and Two-Body Currents on Gamow-Teller Strengths
A. Ekström, G. R. Jansen, K. A. Wendt, G. Hagen, T. Papenbrock, S. Bacca, B. D. Carlsson and D. Gazit
Phys. Rev. Lett. 113, 262504 (2014), e-Print: arXiv:1406.4696

Uncertainty Quantification of the Pion-Nucleon Low-Energy Coupling Constants up to Fourth Order in Chiral Perturbation Theory
K. A. Wendt, B. D. Carlsson and A. Ekström
e-Print: arXiv:1410.0646

Accurate nuclear radii and binding energies from a chiral interaction
A. Ekström, G. R. Jansen, K. A. Wendt, G. Hagen, T. Papenbrock, B. D. Carlsson, C. Forssén, M. Hjorth-Jensen, P. Navrátil and W. Nazarewicz
Phys. Rev. C 91, 051301(R) (2015), e-Print: arXiv:1502.04682

Contents

Chapter 1

Introduction

The purpose of theoretical physics is to understand the physical world around us, usually through the use of mathematical models. From that understanding one aims to make predictions with known precision. Low-energy nuclear physics, which studies the interaction between nucleons at low energy, is at a stage where we are confident about the underlying theory – quantum chromo dynamics (QCD) – governing such systems. However, QCD can not be directly applied at low energies as it is non-perturbative in that region. Instead, another prescription to go from QCD to predictions for low-energy observables is needed. For this we need a model, and numerical methods used to calculate physically relevant quantities – observables – using that model. An important quality of a model is that it has large predictive power. The topic of this Thesis is making predictions using the model chiral effective field theory (χEFT) with accompanying numerical methods. The focus will be on quantifying and improving the predictive power.

According to the scientific method, if the theoretical predictions do not agree with experimentally measured values, the theory either needs to be improved or a new theory needs to be developed. However, most models contain approximations and assumptions, either because the complete theory is too complex to be usable or because some aspects of the theory are not well enough understood. If approximations or assumptions are made – either in the model or in the methods – it is important to know how large effects these will have on the predictions. That is, error bars are needed for the calculated values. Without such error estimates, the model together with the methods used will have little predictive power. A lack of error estimates will in turn make it hard, or even impossible, to falsify the model, which goes

against the principles of the scientific method.

The interaction between nucleons results from the combined effect of the strong and the electromagnetic (EM) forces. The nucleons are colorless bound states of quarks and gluons. The gluons mediate the strong force, while the EM force is carried by the photons. Thus, the most exact model known for the nucleon interaction is obtained by considering all the constituent quarks. However, since this is a very complex model, there is no accurate method for doing actual calculations. The most prominent method, lattice QCD, produces results with large uncertainties and requires large extrapolations as it relies on the use of unphysically large quark masses [1].

There also exist phenomenological interaction models for the description of the nuclear interaction, e.g. the meson-exchange model CD-Bonn [2] and δ-shell interactions [3]. These, and other phenomenological models, are parametrized by a set of free parameters. The free parameters are fixed by fitting the model to selected experimental data. The downside of this approach is that the approximations made are hard to quantify. The model may reproduce the experimental data that is used to fix the free parameters, but there is no telling how good or bad it will perform for other types of experimental data, thus reducing the predictive power of the model.

In between brute-force QCD calculations (which would have a high predictive power but are practically too demanding) and the phenomenological models (which have a too low predictive power) is χEFT. This is an effective, low-energy theory based on QCD, in which nucleons and pions are the effective degrees of freedom instead of the quarks. The basic idea is to first construct the most general Lagrangian, consistent with the symmetries of QCD. This procedure will result in the appearance of contact interactions and pion-exchange terms. The resulting Feynman diagrams are then ordered by an assigned scaling, known as *power counting*. This ordering allows for a systematic improvement of the interaction that in theory enables systematical errors to be under control.

Another important feature of χEFT, which also improves the predictive power, is that both nucleon and pion physics are described by the same model. Experimental data for all of these systems can then be used to constrain, or falsify, the model.

Since χEFT is an effective theory, it is parametrized by low-energy constants (LECs). If precise enough QCD calculations could be made, the values of the LECs could be inferred from such results. As this is currently not possible, a fit to experimental data is used instead.

As a summary, the features that make χEFT a good model with large predictive power are:

- A clear connection to the underlying theory, QCD.
- The ordering of the Feynman graphs allows for systematic improvements and a way to estimate the systematical errors of the model.
- The same model is used to describe both the two-nucleon, the many-nucleon as well as the the pion-nucleon interaction.

This short overview of the available models for the interaction of nucleons highlights only part of the motivation behind this work. The main motivation is that, although χEFT has been used for a long time, the advantages of the model listed above have not been fully exploited. Thus, the real importance of this work is to help remedy this and pave the way for improved nuclear calculations with well-founded error estimates. Here, this is achieved through the use of improved tools and methods including newly developed techniques to calculate observables and their corresponding model errors. This thesis contains:

- Efficient calculation of potential matrix elements (see Sec. 3.1).
- Fast and accurate few and many-body methods to calculate different observables with the method errors under control (see Ch. 3).
- High-precision derivatives up to second order using automatic differentiation (see Sec. 3.2) including specialized routines for various matrix operations.
- Efficient optimization algorithms used to fit the interactions to experimental data (see Ch. 4).
- Sophisticated regression methods and statistical analyses to get statistical uncertainties and correlations for LECs and observables (see Secs. 4.4 and 4.5).

The goal of this thesis is to give a description of χEFT and the methods involved starting from the definition of the interaction to actual predictions of observables.

The thesis is organized as follows. Ch. 2 will focus on the definition of the model – χEFT – and its properties. This includes how to define a non-relativistic potential and how model errors can be estimated. In Ch. 3 the methods used to calculate various observables are presented together with the experimental data. In Ch. 4 we show how actual interactions are constructed from χEFT, how the LECs are determined from a fit to experimental data and how statistical uncertainties are propagated. In Ch. 5 we will put everything together and showcase some results as a proof-of-concept. Finally, in Ch. 6 we will discuss the results and explore some future applications enabled by this work.

Chapter 2

χEFT – The model

This Chapter will focus on the definition and construction of the chiral interaction. For more details see e.g. Refs. [4, 5].

In χEFT nucleons and pions are used as the *effective* degrees of freedom instead of the constituent quarks and gluons. This is a valid approach since the nucleons and pions do not break up into new particles at low energies. χEFT will obey all the symmetries of the underlying theory, QCD, by construction.

Of special interest is the explicitly and spontaneously broken chiral symmetry [4]. If the quarks were massless, chiral symmetry would be an exact symmetry. Due to their small (compared to nucleons) but non-vanishing masses, chiral symmetry is explicitly broken by QCD. It is still, however, an approximate symmetry and one therefore expects to see almost degenerate isospin states and parity states in the hadronic spectrum. This is the case for isospin, e.g. the masses of the neutron and proton are about the same. However, degenerate parity states are not observed in nature [4], implying a spontaneous symmetry breaking. These characteristics determine, to a large extent, how the pions and nucleons interact at low energy, which is then incorporated into χEFT.

Once the symmetries are known, one constructs the most general Lagrangian for the interaction between the nucleons and pions [6] that is consistent with these symmetries. This *effective Lagrangian* will contain an infinite amount of terms, or diagrams, as more and more intermediate states are involved. Furthermore, when the strength of a contribution is not fixed by the underlying symmetries that part will be proportional to a LEC. This means that the more diagrams we include, the more LECs will have to be

determined from data, which in itself is a reduction of the predictive power of the model. To solve this, a *power counting (PC) scheme* is needed, i.e. a way to order the diagrams such that the ones that have the largest impact on the low-energy physics are included first. In this way, we can stop including more diagrams once the desired accuracy is achieved.

The importance of the PC cannot be overstated. If we cannot predict that some diagrams will only have a very small impact on the results, we will have no way to estimate the accuracy of the model without including all of the infinitely many terms. A correct PC should also minimize the amount of LECs needed to achieve a given accuracy. This is important as we will show in Ch. 4 that too many LECs can lead to both a decreased predictive power and a decreased precision of the model.

In this Chapter, we will first define the PC in Sec. 2.1. Then the interaction will be defined in more detail in Secs. 2.2 and 2.3. Finally, we will show how to construct model errors in Sec. 2.4.

2.1 Scales in χEFT

The PC is needed to identify which diagrams are the most important for low-energy interactions. The first question to ask is: what is meant by "low energy"? When nucleons and pions interact with high enough relative momentum p, there could be enough energy to create new particles, such as a ρ meson. This can not be predicted by a χEFT where only pions and nucleons are considered. Therefore, the *breakdown scale* Λ_χ of χEFT– i.e. the energy at which the effective-field theory becomes invalid – is around the mass of the ρ meson, $M_\rho \approx 800\,\text{MeV}$. This sets an upper energy scale for χEFT. On the other hand, the pion masses ($\sim 140\,\text{MeV}$) sets the *characteristic scale* for pion exchanges. The relative momentum p will then be of the order of the pion masses in a low-energy interaction. The PC is then the ordering of the terms in the Lagrangian in powers of Q/Λ_χ, where Q is the *soft scale* given by the pion masses and p, while Λ_χ is the breakdown scale. All terms in the Lagrangian scale according to $(Q/\Lambda_\chi)^\nu$ where $\nu \geq 0$ for all terms allowed by the underlying symmetries. One complication is that there are several other relevant scales involved in the interactions, such as relativistic corrections. In order to have control of the size of the omitted terms, it is vital to include these other scales in an *extended PC*.

One scale is introduced by the nucleon mass $M_N \equiv 2M_pM_n/(M_p + M_n)$

where M_p and M_n is the proton and neutron mass, respectively. The use of the heavy baryon chiral perturbation theory [4, 7] introduces relativistic corrections with factors of $1/M_N$ [4]. We use the power counting introduced by Weinberg (WPC) [8, 9], which means $Q/M_N \approx (Q/\Lambda_\chi)^2$. An alternative power counting used by Machleidt et al. is $Q/M_N \approx Q/\Lambda_\chi$ [4], which results in relativistic corrections entering at lower orders.

The mass difference of the up and down quark gives rise to isospin-breaking effects. These effects will make the proton-proton (pp), neutron-proton (np) and neutron-neutron (nn) interactions slightly different. The effects are proportional to powers of $(m_d - m_u)/(m_d + m_u)$ where m_d and m_u is the mass of the down and up quark, respectively. In order to include this in the extended PC, these effects are assumed to scale as [4]

$$\frac{m_d - m_u}{m_d + m_u} \approx \frac{1}{3} \approx \frac{Q}{\Lambda_\chi}. \tag{2.1}$$

As the nucleons and pions consists of charged quarks, the nucleons and pions also interact with the electro-magnetic (EM) force through the exchange of photons. The EM interaction contributes both with short-range effects, such as isospin breaking due to the different charges, and long-range effects such as the Coulomb interaction. The EM interaction is calculated as an expansion in α, the fine-structure constant, and is incorporated in the extended PC using the approximation [4]

$$4\pi\alpha \approx \frac{1}{10} \approx \left(\frac{Q}{\Lambda_\chi}\right)^2. \tag{2.2}$$

The long-range effects, as the name suggests, become increasingly important as the energy gets lower. Therefore those terms are included at all orders in the chiral expansion.

To conclude, there are four scales involved in the extended PC, with the scaling of a given diagram given as

$$\begin{aligned}\left(\frac{\{m_\pi, p\}}{\Lambda_\chi}\right)^{\nu_\chi} \left(\frac{\{m_\pi, p\}}{M_N}\right)^{\nu_M} \left(\frac{m_d - m_u}{m_d + m_u}\right)^{\nu_q} (4\pi\alpha)^{\nu_\alpha} \\ = \left(\frac{Q}{\Lambda_\chi}\right)^{\nu_\chi + 2\nu_M + \nu_q + 2\nu_\alpha}\end{aligned} \tag{2.3}$$

with $\nu = \nu_\chi + 2\nu_M + \nu_q + 2\nu_\alpha$ and the ν_x being non-negative integers.

With the extended PC firmly in place, we can construct a series of interactions with increasing accuracy by successively raising the upper limit on ν on the included diagrams. This is done in the following two Sections for the nucleons and the nucleon-pion interaction respectively.

2.2 The nucleon interactions

In this Section we will briefly describe the different contributions to the nucleon-nucleon (NN), three-nucleon (3N) and four-nucleon (4N) interactions of strong force origin. The terms, or diagrams, of the interaction are divided into different groups, both depending on the order ν and on the type and quantities of the exchanged particles.

The lowest order interaction is leading order (LO), and consists of all $\nu = 0$ terms. There are no terms with $\nu = 1$ due to parity and time-reversal invariance. Therefore the next-to-leading order (NLO) is constructed from all terms with $\nu \leq 2$. From there on it continues with next-to-next-to-leading order (N2LO or NNLO) being $\nu \leq 3$ and N3LO is $\nu \leq 4$.

The diagrams where only photons are exchanged are the EM interaction, i.e. when only $\nu_\alpha > 0$ using the notation of Eq. (2.3). All other terms are considered part of the strong nuclear interaction. It is usually divided into two parts, the contact interaction (V_{ct}), and the pion exchanges where one or more pion is exchanged ($V_{1\pi}$, $V_{2\pi}$, $V_{3\pi}$, and so on). The pion exchanges are the long-range part of the nuclear interactions and are partially determined by chiral symmetry. The contact interaction, on the other hand, is a general parametrization of the short-range physics, with each term proportional to an LEC. One part of the short-range physics is diagrams involving the Δ-excitation of the nucleon (Δ baryons), which in our model is implicitly a part of the contact interaction.

The contact and pion-exchange diagrams entering the interaction at the different orders are shown in Fig. 2.1. The nucleons and pions are shown with solid and dashed lines, respectively. At LO the leading contact interaction enters, represented by two crossing nucleon lines, and one-pion exchange (1PE). At NLO there are additional contact interactions and also the leading two-pion exchange (2PE). At N2LO there are corrections to the 2PE and also the leading 3N force appears, consisting of contact interactions and pion exchanges. Finally at N3LO there are many new contributions to the contact interaction and the 2PE. The first 4N diagrams also enters at this order. The

three-pion exchange (3PE) appears in both the NN, 3N and 4N interactions. The first relativistic corrections enters at N3LO in our PC.

The order ν_χ of a contact or pion exchange diagram without *spectator particles* (particles that not interact with any other particles) is [4]

$$\begin{aligned} \nu_\chi &= 2A - 4 + 2l + \sum_i \Delta_i \\ \Delta_i &= d_i + \frac{n_i}{2} - 2. \end{aligned} \tag{2.4}$$

Here, A is the number of nucleons, l is the number of pion loops, d_i is the number of derivatives of pion mass insertions and n_i is the number of nucleons entering or leaving vertex i. Δ_i is non-negative for all diagrams allowed by chiral symmetry.

Using this formula, the lowest ν_χ allowed when A nucleons interact is obtained when $l = 0$ and $\sum_i \Delta_i = 0$, i.e. $\nu_{A-N}^{(\min)} = 2A - 4$. Thus, the NN force enters at LO and the 3N force at NLO. However, at NLO all 3N contributions cancel and the first non-vanishing contribution enters at N2LO [10].

2.2.1 The nucleon-nucleon potential

For the calculation of NN scattering we solve the non-relativistic Lippmann-Schwinger (LS) equation and for the calculation of nucleon bound-state observables we employ the non-relativistic Schrödinger equation. In both cases a *non-relativistic potential* is needed. For details on how this potential is constructed from the effective Lagrangian, see e.g. Ref.[4].

A pure NN contact term is an interaction between two nucleons without any exchanged particles. Due to parity, the order ν_{ct} must be even and will in this case only consist of derivative insertions. The contact diagrams are shown in Fig. 2.1.

When M pions are exchanged between two nucleons, it will necessarily involve $L = M - 1$ loops, therefore the leading M-pion exchange will have $\nu_{M-\pi}^{(\min)} = 2M - 2$.

With this power counting, and including the long-range EM interaction

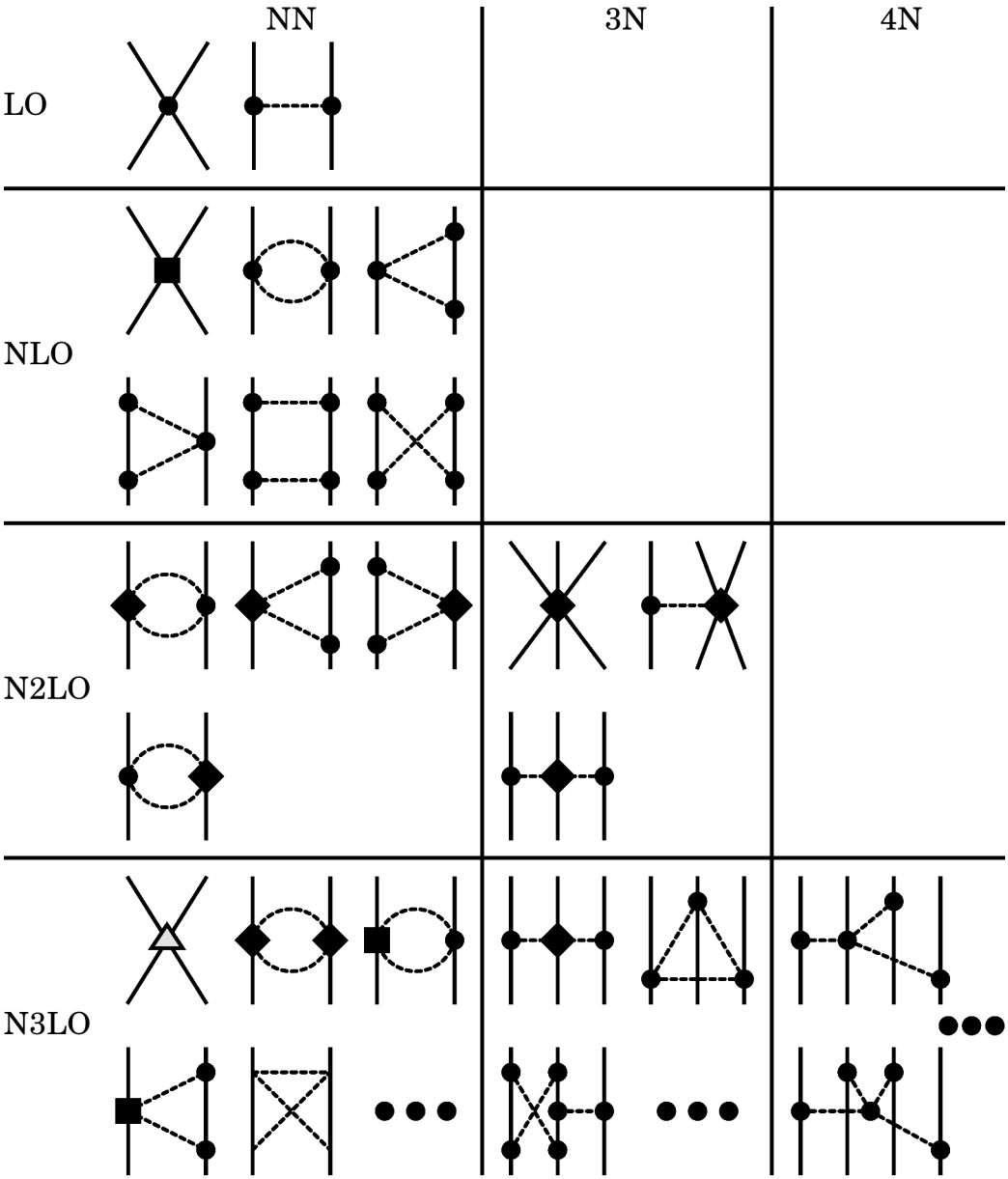

Figure 2.1: Feynman diagrams for the contact and pion-exchange diagrams entering at different orders. Solid (dashed) lines denotes nucleons (pions). A circle, diamond, square and triangle represents a vertex of order $\Delta = 0, 1, 2, 4$ *respectively. Three dots implies that there are more diagrams not shown.*

at all orders, we define the NN potentials at different orders as

$$\begin{aligned} V^{(\mathrm{LO})} &= V_{\mathrm{EM}} + V_{\mathrm{ct}}^{(\mathrm{LO})} + V_{1\pi}^{(\mathrm{LO})} \\ V^{(\mathrm{NLO})} &= V^{(\mathrm{LO})} + V_{\mathrm{ct}}^{(\mathrm{NLO})} + V_{2\pi}^{(\mathrm{NLO})} \\ V^{(\mathrm{N2LO})} &= V^{(\mathrm{NLO})} + V_{2\pi}^{(\mathrm{N2LO})} \\ V^{(\mathrm{N3LO})} &= V^{(\mathrm{N2LO})} + V_{\mathrm{ct}}^{(\mathrm{N3LO})} + V_{2\pi}^{(\mathrm{N3LO})} + V_{3\pi}^{(\mathrm{N3LO})} \end{aligned} \tag{2.5}$$

The 1PE is fully determined by chiral symmetry, and thus does not depend on any LECs. At NLO the leading 2PE enters, see Fig. 2.1. This contribution does not depend on any LECs since all vertices must have index $\Delta = 0$. At N2LO the sub-leading 2PE enters with diagrams proportional to the πN LECs c_1, c_3 and c_4. At N3LO the πN LECs c_2, $d_1 + d_2$, d_3, d_5 and $d_{14} - d_{15}$ enter.

The loops in the 2PE need to be regulated, and this is usually done either using dimensional regularization (DR) or spectral function regularization (SFR) [10]. Here we use the latter, with a regulator parameter $\tilde{\Lambda} = 700\,\mathrm{MeV}$ as an energy cut off. The expressions for the pion exchange contributions in a momentum basis and using SFR can be found in Ref. [5].

The 3PE terms entering at N3LO, see Fig. 2.1 have been shown to be rather small [4] and are therefore ignored.

The contact interaction can be parametrized in different ways. In our calculations we will use a partial-wave momentum-basis. A *channel* in this basis is denoted as ${}^{2S+1}L_J$, where S is the total spin, L the orbital angular momentum (with $L = 0, 1, 2$ denoted by S, P, D and so on) and J the total angular momentum. A convenient parametrization is then given by parameterizing each partial wave independently. At order ν_{ct}, only partial waves up to angular momentum $L + L' = \nu_{\mathrm{ct}}$ will have a non-zero contribution, where L (L') is the incoming (outgoing) orbital angular momentum. Thus, the leading-order contact interaction, $V_{\mathrm{ct}}^{(\mathrm{LO})}$, affects only S-waves, proportional to the NN LECs $\tilde{C}_{^1S_0}$ and $\tilde{C}_{^3S_1}$ The terms from the NLO (N3LO) contact interactions are proportional to the C_x (D_x) NN LECs. For more details, see e.g. Ref. [4]. For the NLO and N3LO contact interactions there are 7 and 15 NN LECs needed to parametrize the contact interaction, respectively.

To sum up the LEC dependence of the different parts in Eq. (2.5), they

all contain terms either proportional to or independent of LECs,

$$\begin{aligned}
V_{\text{ct}}^{(\text{LO})} &\sim \{\tilde{C}_{^1S_0}, \tilde{C}_{^3S_1}\} \\
V_{\text{ct}}^{(\text{NLO})} &\sim \{C_{^1S_0}, C_{^3S_1}, C_{^3S_1-^3D_1}, C_{^3P_0}, C_{^1P_1}, C_{^3P_1}, C_{^3P_2}\}, \\
V_{\text{ct}}^{(\text{N3LO})} &\sim \{D_{^1S_0}, \hat{D}_{^1S_0}, D_{^3S_1}, \hat{D}_{^3S_1}, D_{^3S_1-^3D_1}, \hat{D}_{^3S_1-^3D_1}, D_{^3P_0}, D_{^1P_1}, \\
&\qquad D_{^3P_1}, D_{^3P_2}, D_{^3P_2-^3F_2}, D_{^3D_1}, D_{^1D_2}, D_{^3D_2}, D_{^3D_3}\}, \\
V_{1\pi}^{(\text{LO})} &\sim 1, \\
V_{2\pi}^{(\text{NLO})} &\sim 1, \\
V_{2\pi}^{(\text{N2LO})} &\sim \{c_1, c_3, c_4\}, \\
V_{2\pi}^{(\text{N3LO})} &\sim \{1, d_1+d_2, d_3, d_5, d_{14}-d_{15}, c_1^2, c_2^2, c_3^2, c_4^2, c_1c_2, c_1c_3, c_2c_3\},
\end{aligned} \tag{2.6}$$

More details will be provided in Sec. 3.1.

The various isospin-breaking effects that exist are well described in e.g. Refs. [4, 10]. In short, at LO there are no such effects. At NLO, we get a splitting of the $\tilde{C}_{^1S_0}$ contact into three different contacts, $\tilde{C}_{^1S_0}^{(\text{pp})}$, $\tilde{C}_{^1S_0}^{(\text{np})}$ and $\tilde{C}_{^1S_0}^{(\text{nn})}$. At NLO we also take into account the pion mass splitting in 1PE. This means that $V_{1\pi}$ will be

$$V_{1\pi}^{(\text{pp})} = V_{1\pi}^{(\text{nn})} = V_{1\pi}^{(\text{LO})}(m_{\pi^0}) \tag{2.7}$$

$$V_{1\pi}^{(\text{np},T=0)} = -V_{1\pi}^{(\text{LO})}(m_{\pi^0}) - 2V_{1\pi}^{(\text{LO})}(m_{\pi^\pm}) \tag{2.8}$$

$$V_{1\pi}^{(\text{np},T=1)} = -V_{1\pi}^{(\text{LO})}(m_{\pi^0}) + 2V_{1\pi}^{(\text{LO})}(m_{\pi^\pm}) \tag{2.9}$$

At N2LO we have no additional isospin-violating effects. Most of the isospin-violating effects at N3LO are ignored because they have been shown to be small [4]. The only effect included in our calculations is the pion-photon ($\pi\gamma$) exchange term [11].

At NLO, in addition to the splitting of the 1PE, there are further corrections such as the Goldberger-Treiman discrepancy. This is accounted for by altering the value of the axial-vector coupling constant g_A. At LO, the experimentally determined value of $g_A^{(\text{LO})} = 1.276$ [12] is used and at higher orders a corrected value is used, $g_A^{(\text{NLO,N2LO,N3LO})} = 1.29$ [4].

When the magnitude of an ingoing or outgoing momentum $\boldsymbol{p}$ approaches the breakdown scale Λ_χ of χEFT, the non-relativistic potential V is no longer accurate and it would cause the LS equation to diverge. Therefore, we need to cut off high momentum contributions in the potential. This is done using

a regulator function $f_{\mathrm{NN}}(p)$,

$$V(\boldsymbol{p}', \boldsymbol{p}) \leftarrow V(\boldsymbol{p}', \boldsymbol{p}) f_{\mathrm{NN}}(p') f_{\mathrm{NN}}(p), \tag{2.10}$$

with

$$f_{\mathrm{NN}}(p) = \exp\left[-\left(\frac{p}{\Lambda}\right)^{2n}\right] \tag{2.11}$$

where Λ is a regulator parameter. We use $\Lambda = 500\,\mathrm{MeV}$ and $n = 3$ at all orders. The purpose of the cutoff function is to remove the high-momentum part of the interaction. Since the regulator function is chosen more or less arbitrary and has no physical meaning it should not affect the low-energy physics. However, through correlations between high- and low-momentum states, there will be some degree of alteration of the low-energy physics. This is solved by also modifying the values of the LECs in such a way as to keep the low-energy physics unaltered. Therefore, different regulator functions will require slightly different values of the LECs to make the results cutoff independent.

The electro-magnetic interaction

The electro-magnetic interaction is the part of the nucleon interaction that only involves the exchange of photons. This is the longest range part of the interaction. In this work we use

$$V_{\mathrm{EM}}^{(\mathrm{pp})} = V_{\mathrm{C1}} + V_{\mathrm{C2}} + V_{\mathrm{VP}} + V_{\mathrm{MM}}^{(\mathrm{pp})} \tag{2.12}$$

$$V_{\mathrm{EM}}^{(\mathrm{np})} = V_{\mathrm{MM}}^{(\mathrm{np})} \tag{2.13}$$

where C1 is the static Coulomb interaction, C2 is relativistic corrections to the Coulomb interaction, VP is vacuum polarization [13] and MM the magnetic moment interaction [14]. The long-range effects become increasingly important as the energy approaches zero, therefore we include all long-range effects at all orders in the chiral expansion.

2.2.2 The three-nucleon interaction

The first non-vanishing 3N diagrams appear at N2LO, see Fig. 2.1. It is, therefore, expected to be much smaller than the NN interaction that enters

already at LO. The 3N interaction consists of a 2PE part proportional to the πN LECs c_1, c_3 and c_4, a 1PE part proportional to the 3N LEC c_D and a 3N contact interaction proportional to the 3N LEC c_E [15]. c_D and c_E do not appear in the NN part. At N3LO there are corrections to the N2LO interaction. However, these corrections do not involve any new LECs. The N2LO and N3LO part of the 3N potential in a momentum-space partial-wave basis are presented in Refs. [15] and [16] respectively.

The 3N force, just like the NN force, needs to be regulated to cut off unphysical high-momentum states. This is done using the regulator

$$V \leftarrow V f_{3N}(p', q') f_{3N}(p, q), \tag{2.14}$$

where p and q here are the Jacobi momenta and

$$f_{3N}(p, q) = \exp\left[-\left(\frac{4p^2 + 3q^2}{4\Lambda^2}\right)^n\right] \tag{2.15}$$

where we use the same values $\Lambda = 500\,\text{MeV}$ and $n = 3$ as for the NN potential.

2.2.3 The four-nucleon interaction

For a complete N3LO potential the leading 4N interaction is needed, see Fig. 2.1. The N3LO 4N diagrams consist of four-pion exchanges (4PE), 3PE, 2PE with one NN contact, and 1PE with two NN contacts, all vertices with index $\Delta = 0$. Due to the difficulty of including it in many-body calculations, and because it is expected to be small, it is often neglected.

2.3 The pion-nucleon interaction

One of the advantages of χEFT is that it links NN physics with πN physics. This means that the πN interaction can constrain the pion-exchange part of the NN interaction. The lowest order terms in the πN interaction have $\nu = 1$ and does not involve any LECs. At order $\nu = 2$ the πN LECs c_1 to c_4 enters. Then $d_1 + d_2$, d_3, d_5 and $d_{14} - d_{15}$ enters at $\nu = 3$ and e_{14} to e_{18} at $\nu = 4$ summing up to a total of 13 πN LECs.

At orders LO and NLO in the NN interaction none of the πN LECs enter. At N2LO however, a connection between the NN and πN interactions is established through the πN LECs c_1, c_3 and c_4 as these LECs affects both the NN, 3N and πN interaction.

For more details regarding the πN Lagrangian and the interaction, see e.g. Refs. [17, 18].

2.4 Model errors

Having control over both the systematic and statistical errors of a model is one of the key ingredients for meaningful predictions. The statistical error of χEFT comes from the fitting procedure, in which the values of the LECs are adjusted to make the model predictions fit with the experimental data. From the uncertainty in the values of the experimental data there will be a statistical uncertainty in the values of the LECs. This will be covered in detail in Ch. 4.

The systematic model error (referred to just as the model error) mainly comes from the omitted Feynman diagrams. Therefore, the model error at a given order can be estimated from the expected size of those diagrams. This immediately suggests that the two-nucleon interaction is more important than the three-nucleon interaction, and so on for many-nucleon interactions.

It is crucial to include the model error when fitting to data. In particular for the data where the experimental uncertainties are smaller than the model error. Without this, the fitting procedure can and should not be expected to result in a χ^2/N_{dof} value of 1, where N_{dof} is the number of degrees of freedom in the fit. Including both the model error and the experimental uncertainty in the fitting procedure also results in improved statistical errors, as these should depend on the total uncertainty for the data.

To quantify the model error we estimate the size of the omitted diagrams. At a given order ν, all diagrams up to $(Q/\Lambda_\chi)^\nu$ are included, which means that the impact of the omitted terms should be $\mathcal{O}((Q/\Lambda_\chi)^{\nu+1})$. This still needs to be converted to an actual number, σ_{model}.

The experimental data we use consists mainly of scattering observables plus some bound-state properties. Scattering observables are associated with a fixed center-of-mass momentum p. The method we have used to include model errors is to assume that the real and imaginary parts of each NN and πN scattering amplitude (see Secs. 3.3 and 3.6) have an error

$$\sigma^{(\text{amp})}_{\text{model,x}} = C_x \left(\frac{p}{\Lambda_\chi}\right)^{\nu+1} \quad , \quad x \in \{\text{NN}, \pi\text{N}\}, \tag{2.16}$$

where C_{NN} and $C_{\pi\text{N}}$ are scaling constants to be determined. This corresponds

to a covariance matrix for the scattering amplitudes of the form $(\sigma^{(\mathrm{amp})}_{\mathrm{model,x}})^2 I$ where I is the unit matrix. This means that we do not take correlations between the scattering amplitudes into account. We have made the choice $Q = p$ to capture the trend of an increasing model error as the energy increases. In this approach the size of the error is the same for each scattering amplitude. Therefore, the values of the amplitudes should all be of the same order. Our analysis shows that this is the case for both NN and πN scattering, see Paper 2.

If all uncertainties are correctly included it can be expected that the total χ^2/N_{dof} is about 1. This should approximately hold also for the NN and πN scattering data separately. Therefore, we determine the scaling constants C_{NN} and $C_{\pi\mathrm{N}}$ by requiring that the partial χ^2-values $\chi^2_{(\mathrm{x})}/N^{(\mathrm{x})}_{\mathrm{dof}}$ for the NN and πN scattering data both be 1. The x, standing for NN or πN, signifies that it is the χ^2 and degrees of freedom only for those data. This leads to an iterative process where first the C_x scaling constants are updated, then the LECs are optimized using these C_x and so on until the process has stabilized. This usually does not require more than three iterations.

For bound-state properties it is not clear how to associate a certain energy scale Q, therefore we do not know of a meaningful way to include model errors for these observables. Since there are only very few bound states with $A \lesssim 4$ this is not too big of an issue. Another issue is that the bound-state properties are not functions of a common quantity as was the case for the scattering observables, which are all functions of the scattering amplitudes.

So far we have discussed the systematical model error coming from the omitted diagrams. In order to define our NN potential we introduced regulating functions f_{NN} and $f_{3\mathrm{N}}$, which in our case depend on Λ, the chosen cutoff value. As stated, the values of low-energy observables should not depend on the exact form of $f_{\mathrm{NN,3N}}$ and this is achieved by making the values of LECs depend on the chosen regulator function. However, this will not remove all regulator-dependence and as the energy increases this error is expected to increase also. This is another source of model errors. Although not investigated in this Thesis, the size of this error has been estimated elsewhere (see e.g. [5]) by varying the value of the cutoff parameter Λ appearing in f_{NN} and $f_{3\mathrm{N}}$. It is not clear how to best construct an actual error band from such a variation. However, it is something that could be used in tandem with the above model error based on the size of the omitted diagrams. This could result in a more complete estimate of the model error. A benefit of this method is that it also provides a model error estimate for

the bound-state properties.

Chapter 3

Calculating observables – The methods

With the model firmly in place, it is time to focus on the other essential part of a theory, namely the numerical methods used to calculate observables. As pointed out already in the introduction, efficient methods with controlled approximations is just as important for meaningful predictions as having a good model. Therefore, the focus of this Chapter is to introduce usable numerical methods with well-defined method uncertainties for the calculation of observables.

For numerical values of physical constants, we use the values from CODATA 2010 [19], unless otherwise stated. For the pion masses and the pion decay constant F_π, which are not present in CODATA 2010, we use values from the Particle Data Group [20] for the masses and the value $F_\pi = 92.4\,\text{MeV}$ for the decay constant [5].

The first step in calculating NN and few-nucleon observables is to obtain the nuclear potential, which will be described in Sec. 3.1. For the fitting of the LECs, and the associated regression analysis, we need to obtain the derivatives of the theoretically calculated observable values with respect to the LECs. The computationally advantageous method to calculate these quantities, *automatic differentiation*, is presented in Sec. 3.2.

The computational methods to calculate the different observables – NN elastic scattering, effective range parameters, bound-state properties and πN scattering – are presented in Secs. 3.3, 3.4, 3.5 and 3.6, respectively. The methods are presented together with uncertainty estimates.

3.1 Nuclear potential matrices

For the calculation of observables, we use the NN potential in a partial-wave momentum-basis. Thus, the two-body matrix elements (MEs) of the form $\langle p'J'L'S'T'T'_z|\,V\,|pJLSTT_z\rangle$ are needed, where p is the relative momentum, J the total angular momentum, L the orbital angular momentum, S the total spin and T (T_z) the total (projected) isospin. Total angular momentum conservation gives $J' = J$. Furthermore, for total spin $S = 0$ and $S = 1$ we have $L = J$ and $|L - J| \leq 1$ respectively. From anti-symmetrization we get $T = 0$ (1) for $L + S$ odd (even). The NN interaction is isospin conserving, $T = T'$. It is, however, T and T_z dependent.

The chiral NN potential in a momentum basis is given in Ref. [5]. For the $\pi\gamma$ exchange diagram appearing at N3LO we use a value of $\bar{\gamma} = 0$ for the renormalization-dependent constant. The most general form of the NN potential is (spin and isospin indices suppressed)

$$V(\boldsymbol{p}', \boldsymbol{p}) = \sum_{n\epsilon\{C,S,LS,T,\sigma L\}} \big[V_n(q,k) + \boldsymbol{\tau}_1 \cdot \boldsymbol{\tau}_2 W_n(q,k)\big] X_n(\boldsymbol{q}, \boldsymbol{k}), \tag{3.1}$$

where $\boldsymbol{q} \equiv \boldsymbol{p}' - \boldsymbol{p}$, $\boldsymbol{k} \equiv (\boldsymbol{p}' + \boldsymbol{p})/2$ and $\boldsymbol{\tau}_{1,2}$ ($\boldsymbol{\sigma}_{1,2}$) are the isospin (spin) operators for the two nucleons. The V_n (W_n) potentials is the isoscalar (isovector) part of the potential. The five operator structures X_n are called central ($X_C = 1$), spin ($X_S = \boldsymbol{\sigma}_1 \cdot \boldsymbol{\sigma}_2$), spin-orbit ($X_{LS} = -i(\boldsymbol{\sigma}_1 + \boldsymbol{\sigma}_2) \cdot (\boldsymbol{q} \times \boldsymbol{k})/2$), tensor ($X_T = (\boldsymbol{\sigma}_1 \cdot \boldsymbol{q})(\boldsymbol{\sigma}_2 \cdot \boldsymbol{q})$) and sigma-orbit ($X_{\sigma L} = (\boldsymbol{\sigma}_1 \cdot (\boldsymbol{q} \times \boldsymbol{k}))(\boldsymbol{\sigma}_2 \cdot (\boldsymbol{q} \times \boldsymbol{k}))$). The explicit isospin dependence in Eq. (3.1) evaluates to $\langle T'T'_z|\,\boldsymbol{\tau}_1 \cdot \boldsymbol{\tau}_2\,|TT_z\rangle = (4T - 3)\delta_{T'T}\delta_{T'_zT_z}$. The partial-wave decomposition of the different terms in Eq. (3.1) are given in Ref. [21]. It is a linear transformation and involves different sums of integrals of the form

$$I_{J,L}(p', p) = \pi \int_{-1}^{1} \mathrm{d}z \big[V(q(z), k(z)) + \boldsymbol{\tau}_1 \cdot \boldsymbol{\tau}_2 W(q(z), k(z))\big] z^L P_J(z), \tag{3.2}$$

where $z = \hat{\boldsymbol{p}}' \cdot \hat{\boldsymbol{p}}$ and $P_J(z)$ are Legendre polynomials.[1] $\hat{\boldsymbol{p}}$ denotes a unit vector in the direction of $\boldsymbol{p}$.

[1] In order to avoid any significant error in these calculations, we use a Gauss-Legendre integration mesh of size 96 for z. For p and p', we use a transformed Gauss-Legendre grid of size 120 where the (p_i, w_i) points of a mesh from $p = 0$ to $p = 2$ are transformed to

$$p_i \mapsto 1000 \tan\left(\frac{\pi}{4} p_i\right) \quad , \quad w_i \mapsto 1000 \frac{\pi}{4} w_i \cos^2\left(\frac{\pi}{4} p_i\right).$$

Instead of dividing the NN potential into different operator structures as in Eq.(3.1), it can be split up according to the LEC dependence. All terms in the NN potential, up to N3LO, are either linear or quadratic in the LECs,

$$V(\boldsymbol{\alpha}) = V_0 + \sum_{i=1}^{N_{\boldsymbol{\alpha}}} \alpha_i V_{\alpha_i} + \sum_{i=1}^{N_{\boldsymbol{\alpha}}} \sum_{j=1}^{N_{\boldsymbol{\alpha}}} \alpha_i \alpha_j V_{\alpha_i \alpha_j}, \tag{3.3}$$

where $\boldsymbol{\alpha}$ is the vector of LECs. This simple LEC-dependence makes the derivatives of the NN potential, with respect to the LECs, readily available. Furthermore, each potential term V_0, V_{α_i} and $V_{\alpha_i \alpha_j}$ only needs to be calculated once. Note that no quadratic terms exist up to and including N2LO.

So far we have only focused on the NN potential. The 3N potential also needs to be decomposed into partial waves. This is a more involved and computationally heavier task than for the NN potential. However, Eq. (3.3) is valid for the 3N force too, with the explicit decomposition

$$V(\boldsymbol{\alpha}) = V_0 + c_1 V_{c_1} + c_3 V_{c_3} + c_4 V_{c_4} + c_D V_{c_D} + c_E V_{c_E}, \tag{3.4}$$

for the 3N force at N2LO and N3LO. Thus, the 3N partial-wave decomposition only needs to be done once for V_0 and each V_{α_i} to obtain both the potential and its derivatives. For exact expressions for the decomposition of the N2LO and N3LO contributions to the 3N force, see Refs. [15, 16], while Ref. [22] provides a more general description.

With the MEs and their derivatives calculated we can soon turn to the specific methods for different observables. First, however, some general words about how derivatives for the observables are obtained.

3.2 Automatic differentiation

In Sec. 3.1 we saw that the derivatives of the MEs with respect to the LECs are easy to obtain. However, there are no easy expressions for the derivatives of the observables as functions of the LECs. We need to calculate the derivatives

$$\begin{aligned} &\frac{\partial O_k^{(\text{theo})}(\boldsymbol{\alpha})}{\partial \alpha_i} \quad , \quad \forall\, k, i \\ &\frac{\partial^2 O_k^{(\text{theo})}(\boldsymbol{\alpha})}{\partial \alpha_i \partial \alpha_j} \quad , \quad \forall\, k, i, j, \end{aligned} \tag{3.5}$$

where k runs over a set of observables. One way of obtaining these is to approximate the derivatives with finite differences. This can be achieved using M evaluations in the vicinity of a point $\boldsymbol{\alpha}_n$, then by taking the correct linear combinations of the computed values, it is possible to single out one derivative or second derivative at a time, while all other derivatives up to a chosen order D are zero.

This method, however, is prone to large numerical errors since differences of large, almost equal, numbers are computed. It will also be very sensitive to the distances between the points, the step size. Apart from these numerical problems, it is also a computationally expensive method. For $D = 2$ and 26 parameters one finds that $M = 377$. In practice it would probably be necessary to use $D = 3$ to achieve a reasonable accuracy, which results in $M = 3653$. For these reasons it is not feasible to use finite difference to obtain accurate results.

Another method, which is computationally superior, is forward-mode automatic differentiation (AD). A computer implementation for calculating $O_k^{(\text{theo})}(\boldsymbol{\alpha})$ will consist of a long chain of simple mathematical operations (for example addition and multiplication), elementary functions (such as sin and exp), or matrix operations. All of these have well defined derivatives, so applying the chain rule all the way from the initialization of the parameters to the observable value, will give us the desired derivatives.

Consider for example the LO calculation of the observable $O_k^{(\text{theo})}(2,1)$, where $O_k^{(\text{theo})}(\tilde{C}_{^1S_0}, \tilde{C}_{^3S_1}) = \tilde{C}_{^1S_0}\tilde{C}_{^3S_1} + \exp(2\tilde{C}_{^1S_0} + \tilde{C}_{^3S_1})$, together with the partial derivative with respect to $\tilde{C}_{^1S_0}$. For clarity, we here use the generic notation $f(x,y) = xy + \exp(2x+y)$, and $f'(x,y)$ for the partial derivative with respect to x. We have

$$\begin{aligned}
f(x,y) \quad &, \quad f'(x,y) \\
x = 2 \quad &, \quad x' = 1 \\
y = 1 \quad &, \quad y' = 0 \\
a = xy = 2 \quad &, \quad a' = x'y + xy' = 1 \\
b = \exp(2x+y) = \exp(5) \quad &, \quad b' = \exp(2x+y)(2x'+y') = 2\exp(5) \\
f(2,1) = a + b = 2 + \exp(5) \quad &, \quad f'(2,1) = a' + b' = 1 + 2\exp(5).
\end{aligned} \tag{3.6}$$

In this way, we get machine-precise derivatives, which is a much higher precision than what finite differences would produce. This can be seen clearly in Fig. 3.1, where also the dependence on the step size for the finite difference method is evident.

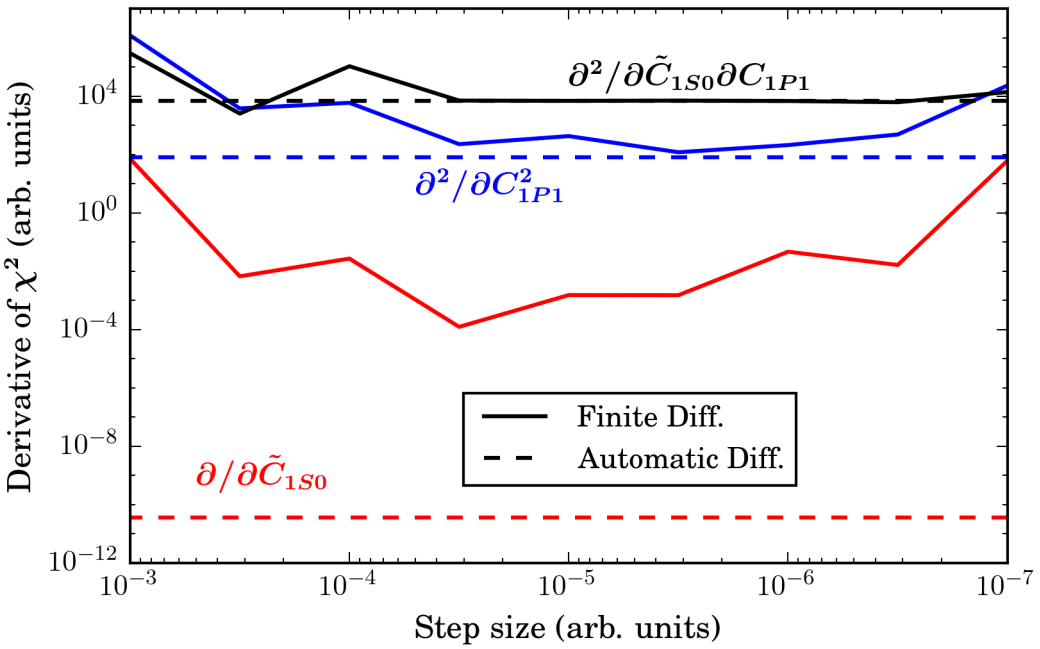

Figure 3.1: Comparison between calculation of first and second derivatives using finite differences (third order) with different step sizes (filled lines) and automatic differentiation (dashed lines). The calculation is done in a minimum where the first derivatives should be approximately zero. Due to cancellation effects the finite difference method can not obtain the low values of the derivatives for any step size. For more details see the text.

To implement forward-mode AD in our code, we use Rapsodia [23] in Fortran. Rapsodia uses derived types with operator overloading and provides overloaded versions of all elementary functions. All real- and complex-valued variables are changed to the corresponding Rapsodia type, and we can then extract the derivatives of the calculated observables. Internally, Rapsodia calculates the derivatives with respect to fixed *directions* $\boldsymbol{d}_i$ in the LEC parameter space. A direction is a linear combination of LECs, $\boldsymbol{d}_i = \sum_j D_{ij}\alpha_j$. The derivatives with respect to $\boldsymbol{d}_i$ are then converted to derivatives of the LECs. This method makes it possible to extract also the mixed second derivatives with respect to the LECs.

For the calculation of first- and second-order derivatives of the LECs, the number of directions needed is

$$N^{(\text{ord}=2)} = \binom{N_{\boldsymbol{\alpha}}(N_{\boldsymbol{\alpha}}+1)}{2} \tag{3.7}$$

which results in $N = 351$ directions for 26 parameters, i.e. 702 extra values are calculated (first- and second derivatives). In our case, this method is still much faster than numerical differentiation for a number of reasons. All calculations that do not depend on the LECs are performed only once, compared to finite difference that would need to do all calculations several times. Also, as seen in Eq. (3.3), all LECs enter only linearly or quadratically in the matrix elements. Therefore, we immediately have the derivatives with respect to the LECs and do not need to use Rapsodia. Therefore, the only workhorses in our calculations are the matrix inversions needed for the computation of NN scattering observables and the solving and setup of the eigenvalue problem in NCSM, which will be covered in more details in Secs. 3.3 and 3.5.

3.3 Nucleon-nucleon elastic scattering

NN elastic scattering observables are calculated from the scattering matrix M [24, 25]. Just like the potential this can be decomposed into partial waves, which is most conveniently done in the singlet-triplet representation of the

scattering matrix,

$$M^{s's}_{m'm}(p,\theta,\phi) = \sum_{J,L,L'} (-1)^{s-s'} i^{L-L'} (2J+1)\sqrt{4\pi(2L+1)}\, Y^{L'}_{m-m'}(\theta,\phi) \cdot \begin{pmatrix} L' & s' & J \\ m-m' & m' & -m \end{pmatrix} \begin{pmatrix} L & s & J \\ 0 & m & -m \end{pmatrix} \frac{\langle L', s' | S^J - 1 | L, s \rangle}{2ip}, \tag{3.8}$$

where the big parentheses are Wigner $3j$-symbols and s (s') and m (m') are initial (final) total spin and spin projection respectively. For a fixed $\boldsymbol{p}$ the M-matrix will be a 4×4 matrix with the basis states $s = 0, m = 0$ and $s = 1, m = -1, 0, 1$. S^J is the 4×4 S-matrix [22] for total angular momentum J. Both the scattering matrix M and the S-matrix satisfy time reversal invariance and parity conservation. Therefore, the S-matrix will be symmetric and only matrix elements with $|L - L'| = 0, 2$ will be non-zero, leaving only six independent quantities. We parametrize these using the *Stapp phase shifts* [26]. This gives

$$S^J_{L=J\pm1} = \begin{pmatrix} e^{2i\delta_{J-1,J}} \cos(2\epsilon_J) & ie^{i(\delta_{J-1,J}+\delta_{J+1,J})} \sin(2\epsilon_J) \\ ie^{i(\delta_{J-1,J}+\delta_{J+1,J})} \sin(2\epsilon_J) & e^{2i\delta_{J+1,J}} \cos(2\epsilon_J) \end{pmatrix} \tag{3.9}$$

for the coupled triplet channel, and

$$S^J_{L=J} = \begin{pmatrix} e^{2i\delta_J} \cos(2\gamma_J) & ie^{i(\delta_J+\delta_{J,J})} \sin(2\gamma_J) \\ ie^{i(\delta_J+\delta_{J,J})} \sin(2\gamma_J) & e^{2i\delta_{J,J}} \cos(2\gamma_J) \end{pmatrix} \tag{3.10}$$

for the (coupled) singlet-triplet channel. The phase shifts ϵ_J and γ_J are called mixing angles.

The scattering matrix can similarly be parametrized by six quantities. We use the Saclay parametrization of the M-matrix [24] with the complex *amplitudes* a to f to express the observables,

$$\begin{aligned} M(\boldsymbol{q},\boldsymbol{k}) = \frac{1}{2}\Big\{ & (a+b) + (a-b)(\boldsymbol{\sigma}_1 \cdot \widehat{\boldsymbol{q}\times\boldsymbol{k}})(\boldsymbol{\sigma}_2 \cdot \widehat{\boldsymbol{q}\times\boldsymbol{k}}) \\ & + (c+d)(\boldsymbol{\sigma}_1 \cdot \hat{\boldsymbol{q}})(\boldsymbol{\sigma}_2 \cdot \hat{\boldsymbol{q}}) + (c-d)(\boldsymbol{\sigma}_1 \cdot \hat{\boldsymbol{k}})(\boldsymbol{\sigma}_2 \cdot \hat{\boldsymbol{k}}) \\ & - e(\boldsymbol{\sigma}_1 + \boldsymbol{\sigma}_2) \cdot \widehat{\boldsymbol{q}\times\boldsymbol{k}} - f(\boldsymbol{\sigma}_1 - \boldsymbol{\sigma}_2) \cdot \widehat{\boldsymbol{q}\times\boldsymbol{k}} \Big\}, \end{aligned} \tag{3.11}$$

where $\boldsymbol{q} \equiv \boldsymbol{p}' - \boldsymbol{p}$ is the momentum transfer and $\boldsymbol{k} \equiv (\boldsymbol{p}' - \boldsymbol{p})/2$ is the average momentum. $\boldsymbol{\sigma}_1$ and $\boldsymbol{\sigma}_2$ are the spin operators for nucleon 1 and 2, respectively. The amplitudes a to f are related to the singlet-triplet representation through linear combinations [25]. For scattering of identical

particles, as in proton-proton scattering, the mixing angles γ_J and the amplitude f will be zero.

Expressions for the different scattering observables as functions of the Saclay parameters can be found in Ref. [24] for identical particles and in Ref. [25] for the more general case of non-identical particles.

The Stapp phase shifts for scattering momentum p_s are calculated from the matrix elements of the free reaction matrix R [2, 22, 27]. It is closely related to the transition matrix T. In a partial-wave momentum-basis, R is determined from a Lippmann-Schwinger-like matrix equation,

$$R = V - VZR. \tag{3.12}$$

V is the partial-wave decomposed potential and Z is a diagonal matrix depending on the scattering momentum p_s.

The infinite sums in Eq. (3.8) are truncated by an imposed upper limit $L_{\max}$ for the angular momenta. The nuclear potential, which is relatively short ranged, only needs $L_{\max} = 35$ to obtain converged results. The long-range electro-magnetic effects, however, need a much higher $L_{\max}$. Since this part of the interaction is independent of all LECs, it is only calculated once. Therefore, we separate the calculation of the short- and long-range contributions to the scattering matrix M. The methods for this will be discussed in the next Section.

3.3.1 Electro-magnetic effects

There are two computational issues with the long-range electro-magnetic contributions. The first is that they are difficult to include at all when using a partial-wave momentum basis, and the second is that they need terms with very high L to converge.

To handle this, the S-matrix is split into different parts using the relation

$$\delta_{V_1+V_2} = \delta_{V_1} + \delta^{V_1}_{V_1+V_2} \tag{3.13}$$

where δ^W_V is the phase shift of the solution of potential V relative to the phase shift of the solution of potential W and the short-hand notation δ_V means relative to a free wave. Thus, the equation above states that the phase shift of the total potential $(V_1 + V_2)$ relative to a free wave is the phase shift of V_1 relative to a free wave plus the phase shift of the total potential relative

to V_1. In the coupled channels this translates to a relationship between S-matrices [14],

$$S_{V_1+V_2} = (S_{V_1})^{\frac{1}{2}}\, S^{V_1}_{V_1+V_2}\, (S_{V_1})^{\frac{1}{2}}\,. \tag{3.14}$$

In np scattering the only long-range interaction is the magnetic moment. The total S-matrix is $S_{\mathrm{MM+N}}$ where N stands for the chiral potential. This is decomposed to

$$S_{\mathrm{MM+N}} = (S_{\mathrm{MM}})^{\frac{1}{2}}\, S^{\mathrm{MM}}_{\mathrm{MM+N}}\, (S_{\mathrm{MM}})^{\frac{1}{2}}\,. \tag{3.15}$$

The factor $S-1$ in the M-matrix expression, Eq. (3.8), is then rewritten to

$$S_{\mathrm{MM+N}} - 1 = (S_{\mathrm{MM}} - 1) + (S_{\mathrm{MM}})^{\frac{1}{2}}\, (S^{\mathrm{MM}}_{\mathrm{MM+N}} - 1)\, (S_{\mathrm{MM}})^{\frac{1}{2}} \tag{3.16}$$

leading to

$$M = M_{\mathrm{MM}} + M_{\mathrm{N}}. \tag{3.17}$$

Since the effect of the magnetic moment interaction is rather small [14], we use the approximation

$$(S_{\mathrm{MM}})^{\frac{1}{2}}\, (S^{\mathrm{MM}}_{\mathrm{MM+N}} - 1)\, (S_{\mathrm{MM}})^{\frac{1}{2}} \approx (S_{\mathrm{N}} - 1). \tag{3.18}$$

The advantage of separating the scattering matrix contribution is that M_{MM} is independent of LECs and can be calculated analytically [14].

For pp scattering it is a bit more involved, since there are more long-range effects, see Eq. (2.12). The splitting of $S_{\mathrm{EM+N}} - 1$ will be

$$\begin{aligned}
S_{\mathrm{EM+N}} - 1 = {} & \left\{S_{\mathrm{C1}} - 1\right\} + (S_{\mathrm{C1}})^{\frac{1}{2}} \left\{S^{\mathrm{C1}}_{\mathrm{C1+C2}} - 1\right\} (S_{\mathrm{C1}})^{\frac{1}{2}} \\
& + (S_{\mathrm{C1}})^{\frac{1}{2}} \left(S^{\mathrm{C1}}_{\mathrm{C1+C2}}\right)^{\frac{1}{2}} \left\{S^{\mathrm{C1+C2}}_{\mathrm{C1+C2+VP}} - 1\right\} \left(S^{\mathrm{C1}}_{\mathrm{C1+C2}}\right)^{\frac{1}{2}} (S_{\mathrm{C1}})^{\frac{1}{2}} \\
& + (S_{\mathrm{C1}})^{\frac{1}{2}} \left(S^{\mathrm{C1}}_{\mathrm{C1+C2}}\right)^{\frac{1}{2}} \left(S^{\mathrm{C1+C2}}_{\mathrm{C1+C2+VP}}\right)^{\frac{1}{2}} \left\{S^{\mathrm{C1+C2+VP}}_{\mathrm{EM}} - 1\right\} \\
& \quad \cdot \left(S^{\mathrm{C1+C2}}_{\mathrm{C1+C2+VP}}\right)^{\frac{1}{2}} \left(S^{\mathrm{C1}}_{\mathrm{C1+C2}}\right)^{\frac{1}{2}} (S_{\mathrm{C1}})^{\frac{1}{2}} \\
& + (S_{\mathrm{C1}})^{\frac{1}{2}} \left(S^{\mathrm{C1}}_{\mathrm{C1+C2}}\right)^{\frac{1}{2}} \left(S^{\mathrm{C1+C2}}_{\mathrm{C1+C2+VP}}\right)^{\frac{1}{2}} \left(S^{\mathrm{C1+C2+VP}}_{\mathrm{EM}}\right)^{\frac{1}{2}} \left\{S^{\mathrm{EM}}_{\mathrm{EM+N}} - 1\right\} \\
& \quad \cdot \left(S^{\mathrm{C1+C2+VP}}_{\mathrm{EM}}\right)^{\frac{1}{2}} \left(S^{\mathrm{C1+C2}}_{\mathrm{C1+C2+VP}}\right)^{\frac{1}{2}} \left(S^{\mathrm{C1}}_{\mathrm{C1+C2}}\right)^{\frac{1}{2}} (S_{\mathrm{C1}})^{\frac{1}{2}}\,.
\end{aligned} \tag{3.19}$$

All EM amplitudes and S matrices are calculated in Coulomb distorted-wave Born approximation (CDWBA), i.e relative to the Coulomb potential. This

is a justified approximation since the C2, VP and MM phase shifts are small and therefore have little interference with each other [14]. As in the np case the magnetic moment is not included in the amplitude involving the chiral potential. These approximations lead to

$$\begin{aligned} S_{\mathrm{EM+N}} - 1 \approx & \left\{S_{\mathrm{C1}} - 1\right\} + \left(S_{\mathrm{C1}}\right)^{\frac{1}{2}} \left\{S^{\mathrm{C1}}_{\mathrm{C1+C2}} - 1\right\} \left(S_{\mathrm{C1}}\right)^{\frac{1}{2}} \\ & + \left(S_{\mathrm{C1}}\right)^{\frac{1}{2}} \left\{S^{\mathrm{C1}}_{\mathrm{C1+VP}} - 1\right\} \left(S_{\mathrm{C1}}\right)^{\frac{1}{2}} \\ & + \left(S_{\mathrm{C1}}\right)^{\frac{1}{2}} \left\{S^{\mathrm{C1}}_{\mathrm{C1+MM}} - 1\right\} \left(S_{\mathrm{C1}}\right)^{\frac{1}{2}} \\ & + \left(S_{\mathrm{C1}}\right)^{\frac{1}{2}} \left(S^{\mathrm{C1}}_{\mathrm{C1+C2}}\right)^{\frac{1}{2}} \left(S^{\mathrm{C1}}_{\mathrm{C1+VP}}\right)^{\frac{1}{2}} \left\{S^{\mathrm{C1+C2+VP}}_{\mathrm{C1+C2+VP+N}} - 1\right\} \\ & \cdot \left(S^{\mathrm{C1}}_{\mathrm{C1+VP}}\right)^{\frac{1}{2}} \left(S^{\mathrm{C1}}_{\mathrm{C1+C2}}\right)^{\frac{1}{2}} \left(S_{\mathrm{C1}}\right)^{\frac{1}{2}} . \end{aligned} \tag{3.20}$$

Then the scattering amplitude can be written as

$$M = M_{\mathrm{C1}} + M_{\mathrm{C2}} + M^{(\mathrm{CDWBA})}_{\mathrm{VP}} + M^{(\mathrm{CDWBA})}_{\mathrm{MM}} + M_{\mathrm{N}}. \tag{3.21}$$

The Coulomb phase shifts σ_L, the C2 phase shifts ρ_L and their corresponding amplitudes have all been worked out and we use the expressions from Stoks et al. [28]. The amplitude M_{C2} is calculated using the limit $L^{(\mathrm{C2})}_{\mathrm{max}} = 1000$. We calculate the vacuum polarization phase shifts in CDWBA, τ_L, using the variable phase method [29]. The values we obtain agree with the ones presented by Bergervoet et al. [30]. The vacuum polarization amplitude is calculated using the approximation derived by Durand [13] including terms up to and including the first order in the expansion parameter $X \equiv 4m_e^2/(T_{\mathrm{lab}} M_p (1 - \cos(\theta_{\mathrm{c.m.}})))$ where m_e is the electron mass and $\theta_{\mathrm{c.m.}}$ is the scattering angle. $X \lesssim 0.031$ for the scattering data we use (see Sec. 3.3.4). The magnetic moment amplitude is given by Stoks[2] [14]. The non-analytical part of the amplitude is calculated using $L^{(\mathrm{MM})}_{\mathrm{max}} = 1000$. In all waves except ${}^1S_0$ we do the approximation

$$S^{\mathrm{C1+C2+VP}}_{\mathrm{C1+C2+VP+N}} \approx S^{\mathrm{C1}}_{\mathrm{C1+C2+VP+N}} \tag{3.22}$$

In ${}^1S_0$, where the magnetic moment interaction is zero, we can write the

[2]Note that Eq. (24) in Ref. [14] has an extra minus and in Eq. (25) it should be $|\sin(\theta)|$.

phase shift as

$$\begin{aligned}
\delta_{\text{C1+C2+VP+N}} &= \delta_{\text{C1}} + \delta^{\text{C1}}_{\text{C1+C2+VP+N}} \\
&= \delta_{\text{C1}} + \delta^{\text{C1}}_{\text{C1+C2}} + \delta^{\text{C1+C2}}_{\text{C1+C2+VP}} + \delta^{\text{C1+C2+VP}}_{\text{C1+C2+VP+N}} \\
&\approx \delta_{\text{C1}} + \delta^{\text{C1}}_{\text{C1+C2}} + \delta^{\text{C1}}_{\text{C1+VP}} + \delta^{\text{C1+C2+VP}}_{\text{C1+C2+VP+N}} \\
\implies \delta^{\text{C1+C2+VP}}_{\text{C1+C2+VP+N}} &\approx \delta^{\text{C1}}_{\text{C1+N}} + \left(\delta^{\text{C1}}_{\text{C1+C2+VP+N}} - \delta^{\text{C1}}_{\text{C1+N}}\right) - \delta^{\text{C1}}_{\text{C1+C2}} - \delta^{\text{C1}}_{\text{C1+VP}} \\
&\equiv \delta^{\text{C1}}_{\text{C1+N}} + \tilde{\Delta}_0 - \rho_0 - \tau_0
\end{aligned} \tag{3.23}$$

where $\tilde{\Delta}_0$ is calculated by interpolating between the values tabulated by Bergervoet et al. [30]. In principle $\tilde{\Delta}_0$ is dependent on the chiral interaction, but the dependence was seen to be very small [30].

Thus, all pp phase shifts we calculate are in CDWBA. Due to the long range of the Coulomb potential it is difficult to directly obtain the phase-shifts of the potential. Therefore we use Vincent-Phatak matching [31]. The idea is to split the total potential V into a short-range potential V_s and a long-range part V_l,

$$V = V_s\theta(R_c - r) + V_l\theta(r - R_c), \tag{3.24}$$

where R_c is a distance chosen such that $V_l \approx V_{\text{C1}}$. The phase-shifts δ_s of V_s can be obtained directly using the R-matrix approach. The full phase-shifts $\delta^{\text{C1}}_{V+\text{C1}}$ are then obtained by matching the asymptotic behavior of the wave function to the Coulomb wave functions.

3.3.2 Derivatives of the R-matrix elements

Most of the calculations needed to obtain the scattering observables are easily adopted to AD to obtain derivatives. The only exception is the R-matrix calculation, which is more efficiently done using explicit formulas. In matrix-form, the LS equation for the R-matrix is (c.f. Eq. (3.12))

$$R = V - VZR \implies (I + VZ)R = V, \tag{3.25}$$

where I is the identity matrix. The above equation can be solved by doing an LU factorization of the matrix $I + VZ$. Derivatives of R with respect to an LEC α_x, denoted R_{α_x}, is then obtained by direct differentiation of the above equation,

$$\begin{aligned}
&V_{\alpha_x}ZR + (I + VZ)R_{\alpha_x} = V_{\alpha_x} \\
&\quad\implies (I + VZ)R_{\alpha_x} = V_{\alpha_x}(I - ZR).
\end{aligned} \tag{3.26}$$

Thus, the same LU factorization which has already been computed can be used to obtain the derivatives also, making the calculations very efficient. The second derivatives are obtained in the same way by applying another derivative,

$$(I + VZ)R_{\alpha_x\alpha_y} = V_{\alpha_x\alpha_y}(I - ZR) - V_{\alpha_x}ZR_{\alpha_y} - V_{\alpha_y}ZR_{\alpha_x}. \tag{3.27}$$

3.3.3 Method error

One source of method uncertainties for the calculation of NN scattering observables is the truncations in $L_{\max}$. Since the calculations of scattering observables are relatively fast, we could choose $L_{\max}$ values large enough that the method uncertainty due to the truncation is much smaller than other sources of uncertainty. Therefore this method error is ignored.

There are, however, more sources of uncertainty. In the inclusion of the long-range EM effects we made a number of approximations. These approximations have all been shown to be small enough that they can be ignored, which is what we do here. See Sec. 3.3.1 for references. However, with new, more exact experimental data and improved accuracy in the theoretical calculations it might be worthwhile to check the accuracy of these approximations again.

We now have a method to calculate any NN elastic scattering observable with known method uncertainties. To compare the theoretical results with experiment, we need experimental data points.

3.3.4 Experimental data

Experimental scattering data is usually measured either at several scattering angles or several energies in the same experiment. For some of these experiments, a common *normalization* $C_{\text{expr}} \approx 1$ with uncertainty σ_C is given by the experimenter together with the N_d experimental values $O_d^{(\text{expr})}$. To account for the common normalization of the data, a parameter C is introduced, called a normalization constant, which is determined by minimizing the sum

$$\left(\frac{C-1}{\sigma_C}\right)^2 + \sum_{d=1}^{N_d}\left(\frac{CO_d^{(\text{theo})}(\boldsymbol{\alpha}) - O_d^{(\text{expr})}}{\sigma_{d,\text{total}}}\right)^2, \tag{3.28}$$

for a fixed set of LECs α. The value of C which minimizes this sum, is

$$C = \frac{\frac{1}{\sigma_C^2} + \sum_{d=1}^{N_d} \frac{O_d^{(\mathrm{theo})} O_d^{(\mathrm{exp})}(\boldsymbol{\alpha})}{\sigma_{d,\mathrm{total}}^2}}{\frac{1}{\sigma_C^2} + \sum_{d=1}^{N_d} \frac{\left(O_d^{(\mathrm{theo})}(\boldsymbol{\alpha})\right)^2}{\sigma_{d,\mathrm{total}}^2}} \tag{3.29}$$

Some of these datasets are *floated*, meaning that the value of the constant C is unconstrained. In these cases, the $(C-1)^2/\sigma_C^2$ term is excluded.

We employ the SM99 database [32] (see Refs. [2, 28, 33] for more details) which consists of 2932 pp data and 3058 np data (including normalization data) up to $T_{\mathrm{lab}} = 350\,\mathrm{MeV}$. Since our theoretical calculations are for elastic scattering, we only consider data up to $T_{\mathrm{lab}} = 290\,\mathrm{MeV}$, which is around the pion production threshold. This means we have $N_{\mathrm{data}}^{(\mathrm{pp})} = 2045$ and $N_{\mathrm{data}}^{(\mathrm{np})} = 2400$ including normalization data. The number of normalization constants are $N_{\mathrm{norm}}^{(\mathrm{pp})} = 124$ and $N_{\mathrm{norm}}^{(\mathrm{np})} = 148$. The number of degrees of freedom in the datasets are $N_{\mathrm{dof}}^{(\mathrm{pp})} \equiv N_{\mathrm{data}}^{(\mathrm{pp})} - N_{\mathrm{norm}}^{(\mathrm{pp})} = 1921$ and $N_{\mathrm{dof}}^{(\mathrm{np})} = 2252$.

Instead of using experimental data to fit the LECs, the phase shifts, defined in Eqs. (3.9) and (3.10) can be used. Phase shift values have been obtained in various analyses, see e.g. Refs. [3, 28]. The benefit of using phase shifts is that they are easier to calculate than the observables and they will decouple most of the NN contact LECs from each other as these only affect one partial wave each. However, since the phase shifts are not real observables it is not possible to assign well-founded uncertainties to the phase shifts. Therefore, a fit to experimental data should be done, which is what we do in this Thesis. A fit to phase shifts can, however, provide good starting points for the subsequent fit to data.

The SM99 database contains no nn data, which means there is no two-body data to constrain the nn part of the interaction. This is remedied by the use of the effective range expansion, which will be described next.

3.4 Effective range parameters

The effective range expansion (ERE) is a parametrization of low-energy phase-shifts [34]. It is most common for the S-waves, where the ERE parameters can be directly compared to experimental data. Since there is no nn scattering data available, the nn ERE parameters are useful quantities to use to constrain the nn part of the interaction, more precisely the LEC $\tilde{C}_{^1S_0}^{\mathrm{nn}}$.

The nn ERE parameters can be obtained from e.g. the $^2\mathrm{H}(\pi^-, n\gamma)n$ capture reaction [35–37]. The other ERE parameters are also useful to calculate to compare to experiment.

The exact form of the ERE depends on which long-range electro-magnetic effects that are included. It can be expressed in the general form

$$A(p) + B(p)p\cot(\delta^{LR}_{LR+N}) = -\frac{1}{a} + \frac{1}{2}r^2p^2 + O(p^4). \tag{3.30}$$

where LR stands for the long-range part. For nn and np scattering there is no long-range electro-magnetic potential, which gives $A(p) = 0$ and $B(p) = 1$ [34]. The corresponding ERE parameters are denoted $a^{\mathrm{N}}_{\mathrm{nn}}$, $a^{\mathrm{N}}_{\mathrm{np}}$, $r^{\mathrm{N}}_{\mathrm{nn}}$ and $r^{\mathrm{N}}_{\mathrm{np}}$, where the N denotes that only the nuclear interaction is included.

When calculating ERE parameters for pp scattering, we include the Coulomb interaction, which means that $\delta^{LR}_{LR+N} = \delta^{C1}_{C1+N}$. In this case, $A(p)$ and $B(p)$ are given by [30, 34]

$$A(p) = A_C(p) = 2p\eta'\left(\mathrm{Re}[\Psi(1+i\eta')] - \log(\eta')\right) \tag{3.31}$$

$$B(p) = B_C(p) = \frac{2\pi\eta'}{\exp(2\pi\eta') - 1} \tag{3.32}$$

$$\eta' = \frac{\alpha}{2p}\frac{M_p^2 + 2p^2}{\sqrt{M_p^2 + p^2}}, \tag{3.33}$$

where $\Psi(z)$ is the digamma function and η' the relativistic Coulomb parameter. These ERE parameters are denoted $a^{\mathrm{C}}_{\mathrm{pp}}$ and $r^{\mathrm{C}}_{\mathrm{pp}}$.

The ERE is linear as a function of p^2 for low p. The ERE parameters are therefore determined using a linear least-squares fit to 20 equally-spaced phase shifts in the range $T_{\mathrm{lab}} = 10 - 100\,\mathrm{keV}$. This is exact enough that the method error for these observables is negligible compared to other uncertainties.

The experimental values and uncertainties for the ERE parameters are presented in Tab. 3.1.

Instead of using the ERE parameters in the nn channel to constrain the nn part of the interaction, it is possible to use bound-state properties of ^{3}H. The bound-state properties will be discussed next.

Table 3.1: Experimental values and errors for the effective range expansion (ERE) parameters (in fm). The superscript N denotes that it is ERE parameters for the nuclear interaction only, while C denotes that the Coulomb interaction is included.

	Experiment	Reference
$a_{\mathrm{nn}}^{\mathrm{N}}$	−18.95(40)	[4]
$a_{\mathrm{np}}^{\mathrm{N}}$	−23.7148(43)	[38]
$a_{\mathrm{pp}}^{\mathrm{C}}$	−7.8196(26)	[30]
$r_{\mathrm{nn}}^{\mathrm{N}}$	2.75(11)	[4]
$r_{\mathrm{np}}^{\mathrm{N}}$	2.750(62)	[38]
$r_{\mathrm{pp}}^{\mathrm{C}}$	2.790(14)	[30]

3.5 Bound-state properties

In addition to scattering observables we calculate binding energies and radii for ^{2}H (deuteron), ^{3}H (triton), ^{3}He (helion) and the ^{4}He (alpha particle). We also compare the quadrupole moment of the deuteron, $Q(^2\mathrm{H})$, and the comparative half-life of triton, $fT_{1/2}(^3\mathrm{H})$. In our fitting procedure, the bound-state observables for $A > 2$ are the only data that can constrain the LECs c_D and c_E in the 3N force.

These observables are calculated using the no-core shell model (NCSM) in a harmonic-oscillator (HO) basis using relative coordinates [39]. The binding energies and wave functions are obtained directly from the eigenvalue problem $\mathcal{H}\,|\Psi_n\rangle = E_n\,|\Psi_n\rangle$, which is solved using exact diagonalization with the LAPACK library [40].

The potential V in an HO basis is obtained from the partial-wave momentum-basis through a linear transformation. This is an integration of the potential MEs together with HO basis functions. These basis functions depend on a chosen oscillator frequency $\hbar\omega$. The HO basis is truncated by an upper limit $N_{\max}$ on the allowed HO excitation level. If $N_{\max} \to \infty$ then the results would be independent on $\hbar\omega$. However, for finite $N_{\max}$ a good choice of the oscillator frequency will yield faster convergence as a function of $N_{\max}$. In our calculations, we use $\hbar\omega = 36\,\mathrm{MeV}$ and $N_{\max}^{(3)} = 40$ for three-body calculations and $N_{\max}^{(4)} = 20$ for four-body calculations.

The experimentally measured *charge mean-squared radius* is related to the theoretically calculated *point-proton mean-squared radius* through the

relation [41]

$$r^2_{\text{pt-p}} = r^2_{\text{ch}} - r^2_p - \frac{N}{Z} r^2_n - r^2_{\text{DF}} - \Delta r^2, \tag{3.34}$$

where r^2_p (r^2_n) is the proton (neutron) charge mean-squared radius and Z (N) is the proton (neutron) number. We use $r_p = 0.8783(86)\,\text{fm}$ and $r^2_n = -0.1149(27)\,\text{fm}^2$ [42]. The term $r^2_{\text{DF}} \equiv \frac{3}{4M^2_N}$ is the Darwin-Foldy correction [43]. The last term in Eq. (3.34) allows possible further corrections coming from two-body currents and relativistic corrections. We do not include such corrections, i.e. we use $\Delta r^2 = 0$.

The electric quadrupole moment calculated from the wave function, just like the radius, needs to be corrected with two-body currents and relativistic corrections in order to be able to compare with experimental data. However, we do not know the size of these corrections. The calculated quadrupole moment for the deuteron is usually too low compared to experiment [4] so we choose to fit against the value obtained by Entem and Machleidts CD-Bonn potential, $Q_{\text{d}} = 0.27$ [4], with an error of 4%. This error is roughly the discrepancy between the calculated and the experimental value.

The comparative half-life of triton is calculated from [44]

$$\left\langle E^A_1 \right\rangle \equiv \left| \left\langle {}^3\text{He} \middle\| E^A_1 \middle\| {}^3\text{H} \right\rangle \right|, \tag{3.35}$$

the reduced matrix element for the $J = 1$ electric multiple of the axial-vector current. This is related to the comparative half-life of triton determined to be $fT_{1/2} = 1129.6 \pm 3\,\text{s}$ [45], leading to the empirical value $\left\langle E^A_1 \right\rangle = 0.6848 \pm 0.0011$ [44].

3.5.1 Method error

In the calculation of bound-state properties with the NCSM, we have a truncation error due to N_{max} that for some observables are comparative or larger than the experimental error. Therefore, we have estimated the truncation error by doing an extrapolation in N for a few potentials, resulting in the adopted method error σ_{method}. The obtained errors together with experimental values and errors for all bound-state observables are presented in Tab. 3.2. In particular, the binding energies have very small experimental uncertainties, resulting in the method error being completely dominating.

Table 3.2: Experimental values and errors for ground-state binding energies (in MeV) and radii (in fm). The quadrupole moment ($Q(^2H)$) of the deuteron is given in fm^2. $E^1_A(^3H)$ is a reduced transition matrix element directly related to the comparative half life.

	Experiment	Reference	$\sigma_{\text{exp+method}}$
$E(^2\text{H})$	−2.22456627(46)	[19]	0.47×10^{-6}
$E(^3\text{H})$	−8.4817987(25)	[19]	3.3×10^{-3}
$E(^3\text{He})$	−7.7179898(24)	[19]	3.8×10^{-3}
$E(^4\text{He})$	−28.2956099(11)	[19]	6.5×10^{-3}
$r_{\text{pt-p}}(^2\text{H})$	1.97559(78)[a]	[42, 46]	0.78×10^{-3}
$r_{\text{pt-p}}(^3\text{H})$	1.587(41)	[42]	0.041
$r_{\text{pt-p}}(^3\text{He})$	1.7659(54)	[42]	0.013
$r_{\text{pt-p}}(^4\text{He})$	1.4552(62)	[42]	7.1×10^{-3}
$Q(^2\text{H})$	0.27(1)[b]		0.01
$E^1_A(^3\text{H})$	0.6848(11)	[44]	1.1×10^{-3}

[a] The experimental value is $r_{\text{d}}^2 - r_p^2$, we still use the value of r_n^2 from ref. [42]
[b] This is not an experimental value, see the text for details.

3.5.2 Derivatives of wave functions and observables

To obtain the binding energies and wave functions from the Hamiltonian, we solved the eigenvalue problem $\mathcal{H}|\Psi_n\rangle = E_n|\Psi_n\rangle$. Since $\mathcal{H}$ is real and symmetric, this results in a decomposition $\mathcal{H}U = U\mathcal{E}$, with $U^TU = I$, where column n of U is the wave function $|\Psi_n\rangle$ and the element $\mathcal{E}_{nn}$ of the diagonal matrix $\mathcal{E}$ is the energy E_n.

Applying AD to the diagonalization directly is not practical. Therefore, we use explicit formulas for the derivatives of the energies and wave functions with respect to the LECs. The computation of the derivatives requires that all energy eigenvalues are distinct [47], which is the case. The condition $U^TU = I$ were I is the identity matrix ensures that that the eigenvectors are orthogonal and normalized to 1. Differentiation with respect to LEC α_x (denoted $\mathcal{H}_{\alpha_x}$) yields

$$\begin{aligned} &\mathcal{H}_{\alpha_x}U + HU_{\alpha_x} = U_{\alpha_x}\mathcal{E} + U\mathcal{E}_{\alpha_x} \\ \Longrightarrow\ &U^T\mathcal{H}_{\alpha_x}U = \mathcal{E}_{\alpha_x} + U^TU_{\alpha_x}\mathcal{E} - \mathcal{E}U^TU_{\alpha_x} = \mathcal{E}_{\alpha_x} + \Delta E \circ (U^TU_{\alpha_x}) \\ &(\Delta E)_{nm} \equiv E_m - E_n, \end{aligned} \tag{3.36}$$

where $\circ$ denotes the Hadamard (element-wise) multiplication of two matrices. Clearly, the first term on the right hand side ($\mathcal{E}_{\alpha_x}$) is diagonal and the other term is zero on the diagonal. Therefore, the derivatives of the energies are the diagonal elements of the matrix on the left hand side,

$$\frac{\partial E_n}{\partial \alpha_x} = \left(U^T \mathcal{H}_{\alpha_x} U\right)_{nn} = \langle \Psi_n | \mathcal{H}_{\alpha_x} | \Psi_n \rangle . \tag{3.37}$$

Now we need to solve for U_{α_x} in Eq. (3.36). We cannot immediately take the Hadamard product with the element wise inverse of ΔE due to the diagonal, which is zero. Since all eigenvalues are distinct, ΔE is zero only on the diagonal. From the normalization condition $U^T U = I$ we get the diagonal elements of $U^T U_{\alpha_x}$,

$$\begin{aligned} I_{\alpha_x,nn} &= (U^T U)_{\alpha_x,nn} = (U_{\alpha_x}^T U)_{nn} + (U^T U_{\alpha_x})_{nn} \\ &= (U^T U_{\alpha_x})_{nn}^T + (U^T U_{\alpha_x})_{nn} = 2(U^T U_{\alpha_x})_{nn} = 0 \end{aligned} \tag{3.38}$$

Since the diagonal of $U^T U_{\alpha_x}$ is zero, we can take the Hadamard product with the matrix F, defined as

$$F_{nm} = \begin{cases} 0 & \text{for} \quad n = m \\ ((\Delta E)_{nm})^{-1} & \text{for} \quad n \neq m, \end{cases} \tag{3.39}$$

in Eq. (3.36) to obtain

$$\begin{aligned} F \circ (U^T \mathcal{H}_{\alpha_x} U) &= U^T U_x \\ \Longrightarrow \quad U_{\alpha_x} &= U(F \circ (U^T \mathcal{H}_{\alpha_x} U)) \\ \Longrightarrow \quad \frac{\partial}{\partial \alpha_x} |\Psi_n\rangle &= \sum_{m \neq 0} \frac{\langle \Psi_m | \mathcal{H}_{\alpha_x} | \Psi_n \rangle}{E_n - E_m} |\Psi_m\rangle . \end{aligned} \tag{3.40}$$

Here we see explicitly why it is important that all energies are distinct when using these expressions for the derivatives. The second derivatives are then obtained by simply applying a second derivative to Eqs. (3.37) and (3.40).

3.6 Pion-nucleon scattering

We also calculate pion-nucleon scattering observables. For experimental values, we employ the database used by the Washington Institute group [48],

here referred to as the WI08 database. We calculate observables up to the lab kinetic energy 70 MeV. This results in $N_{\text{data}}^{(\pi\text{N})} = 1347$ data including normalization data and $N_{\text{norm}}^{(\pi\text{N})} = 110$ [18]. The data consists mainly of differential cross sections and some singly-polarized differential cross sections for the processes

$$\pi^{\pm} + p \to \pi^{\pm} + p \quad \text{and}$$
$$\pi^{-} + p \to \pi^{0} + n.$$

These observables are calculated from the amplitudes f and g. For a description of how the πN amplitudes are constructed, see Ref. [18] and for a more detailed description of the strong and EM amplitudes see Refs [49–53].

Since χEFT is a low-energy theory, we need low-energy data to constrain it. However, the lowest lab energy present in the WI08 database is $T_{\text{lab}} = 10.6$ MeV. This means that the lower order potentials will not be able to accurately describe any of the data in the database. For this reason, we have chosen to include all terms up to and including $\nu = 4$ when calculating πN observables. This will include all c_i, d_i and e_i LECs, in total 13 LECs that affect the πN scattering. The fitting of these LECs and the NN contact LECs to the data described in this Chapter is presented next.

Also for the πN scattering we include enough partial waves so that the estimated method uncertainty is so small that it can be neglected.

Chapter 4

Optimization

In Ch. 2 we defined the model, χEFT. As stressed also in the introduction, we saw that using the same low-energy effective theory it is possible to describe πN, NN and few-nucleon processes. The methods to calculate such observables were described in Ch. 3. To make actual predictions using the model and methods presented, we first need to assign values to the LECs. The LECs parametrize all interactions that obey the underlying symmetries.

Although the theory does not provide definite values for the LECs, it does provide an expected order of magnitude for each LEC. This will be discussed in Sec. 4.1.

In order to constrain the values of the LECs further, a fit to data is done. The idea is to select a set of experimentally determined observables, $O_k^{(\mathrm{expr})}$, and compare them to what the theory predicts, $O_k^{(\mathrm{theo})}(\boldsymbol{\alpha})$, for given values of the LECs, represented by the vector $\boldsymbol{\alpha}$. The LEC values that result in the best agreement between the model and the data, denoted by $\boldsymbol{\alpha}_*$, is then chosen to define the interaction. This statement will be made more precise in Sec. 4.2 where the χ^2-function is introduced.

In Sec. 4.3 the methods used to minimize the χ^2-function are presented. In Secs. 4.4 and 4.5 the resulting statistical analysis is presented, leading to the statistical uncertainties in the calculated observables. Finally, in Sec. 4.6 correlations for LECs and observables are discussed.

4.1 A priori knowledge of the LECs

Already in the model it is implicitly assumed that the values of the LECs are of *natural size*, in order for the power counting to be correct. Otherwise terms at a given order would be too large or too small. LECs can be assumed to be natural if they are of the sizes [5, 15, 17]

$$\begin{aligned}
\tilde{C}_x &\sim \frac{4\pi}{F_\pi^2} \approx 0.15 \times 10^4\,\mathrm{GeV}^{-2} \\
C_x &\sim \frac{4\pi}{F_\pi^2 \Lambda^2} \approx 0.59 \times 10^4\,\mathrm{GeV}^{-4} \\
D_x &\sim \frac{4\pi}{F_\pi^2 \Lambda^4} \approx 2.4 \times 10^4\,\mathrm{GeV}^{-6} \\
c_x &\sim \frac{1}{2M_N} \approx 0.53\,\mathrm{GeV}^{-1} \\
d_x &\sim \frac{1}{4M_N^2} \approx 0.28\,\mathrm{GeV}^{-2} \\
e_x &\sim \frac{1}{8M_N^3} \approx 0.15\,\mathrm{GeV}^{-3} \\
c_{D,E} &\sim 1.
\end{aligned} \tag{4.1}$$

In the numerical approximations, $\Lambda = 500\,\mathrm{MeV}$ was used just as in the regulator function that we employ. When fitting the model to the data we therefore mainly search within two orders of magnitude from these values. The resulting LECs should be of the magnitudes specified in Eq. (4.1), otherwise there might be some wrong assumptions concerning the validity of the χEFT model.

Since each additional contribution from higher orders should only be a small correction for low-energy observables, the values of LECs are not expected to change significantly from order to order.

Furthermore, the nuclear interaction is expected to have an approximate Wigner SU(4) symmetry due to the large scattering lengths in the S-waves [54]. Therefore, the two LO LECs should be of about the same size, $\tilde{C}_{^1S_0} \approx \tilde{C}_{^3S_1}$. If this is not obtained in the fit to data it is a sign that it might be an erroneous minimum.

4.2 The χ^2-function

A common method to use for parameter optimization, which we also use here, is to do a least-squares minimization. This means that the sum of squared residuals, the χ^2-function, is minimized,

$$\chi^2(\boldsymbol{\alpha}) \equiv \sum_{k\in\mathbb{M}} \left(\frac{O_k^{(\text{theo})}(\boldsymbol{\alpha}) - O_k^{(\text{expr})}}{\sigma_{k,\text{total}}} \right)^2 \equiv \sum_{k\in\mathbb{M}} r_k^2(\boldsymbol{\alpha}), \tag{4.2}$$

where $\mathbb{M}$ is a set of fitting observables, which is a subset of the observables presented in Secs. 3.3, 3.4, 3.5 and 3.6. The total error of an observable, $\sigma_{k,\text{total}}$ is defined as the quadratic sum of the uncertainties in the theoretical value and in the experimental value,

$$\sigma_{k,\text{total}}^2 = \sigma_{k,\text{expr}}^2 + \sigma_{k,\text{theo}}^2 = \sigma_{k,\text{expr}}^2 + \sigma_{k,\text{numerical}}^2 + \sigma_{k,\text{method}}^2 + \sigma_{k,\text{model}}^2. \tag{4.3}$$

We have estimated all numerical errors to be much smaller than the other sources of errors, so we ignore $\sigma_{\text{numerical}}^2$. The experimental error is given by the experimenter together with the experimental data. The model error is described in Sec. 2.4. The remaining observable dependent method error was defined in Ch. 3.

Some of the benefits of this type of least-squares minimization is that (i) uncertainties in both the experimental values and the model can be included, (ii) data with different units and magnitudes can easily be included in the same minimization, and (iii) it is possible to propagate the uncertainties used in the fit to statistical uncertainties in LECs and observables together with correlations.

If each $O_k^{(\text{theo})}(\boldsymbol{\alpha}_*)$ and $O_k^{(\text{expr})}$ can be assumed to be normally distributed, with their associated errors as standard deviation and the exact value $O_k^{(\text{exact})}$ as mean, then $r_k \sim \mathcal{N}(0,1)$ for each k, where $\mathcal{N}(\mu,\sigma^2)$ is the normal distribution with mean μ and variance σ^2. If furthermore each theoretical and experimental value can be considered independent of each other, then $\chi^2(\boldsymbol{\alpha}_*)$ will have a chi-squared distribution around the minimum with $N_{\mathbb{M}} - N_{\text{norm}} - N_{\boldsymbol{\alpha}} \equiv N_{\text{dof}}$ degrees of freedom. N_{norm} is the number of free normalization constants in the scattering data as was discussed in Sec. 3.3.

The assumptions about the residuals will not be entirely satisfied for real data and estimated model errors. In particular, if there are large systematical errors in the theoretical calculations, the residuals are not expected to be entirely Gaussian nor entirely independent. This is the case when the

model uncertainty dominate the total error budget. However, this does not invalidate the use of the χ^2-function to fit the parameters, but the minimizing parameter set $\boldsymbol{\alpha}_*$ will not be the maximum-likelihood estimator.

Whether $\chi^2(\boldsymbol{\alpha}_*)$ is chi-squared distributed or not, a minimization of $\chi^2(\boldsymbol{\alpha})$ can still give insight into both the model and the data [55]. It is, among other things, possible to

- determine if the data is sufficient to constrain the model,
- compare different minimization methods,
- probe the models maximal accuracy through a statistical analysis,
- find missing physics in the model.

4.3 Minimization methods and methodology

The actual minimization of $\chi^2(\boldsymbol{\alpha})$ is a non-linear problem. This can be solved in many ways. The methods available can be roughly divided into *local* and *global* optimization methods. The local methods are iterative methods starting with an initial guess $\boldsymbol{\alpha}_0$ to successively find better parameters $\boldsymbol{\alpha}_n$, n $= 1, 2, \ldots$, until a *local minimum* is found. Which local minimum that is found is strongly dependent on $\boldsymbol{\alpha}_0$. Global optimization methods does not need starting parameters $\boldsymbol{\alpha}_0$. Instead they search the entire allowed parameter space to find the global minimum.

For the fitting of the LECs it has been sufficient to use local optimization methods. The benefit of these methods is that they can efficiently and reliably find a local minimum given a good starting point. The downside is that extra care needs to be taken to make sure the correct local minimum is found.

We have used three local minimization methods: POUNDerS [56], Levenberg-Marquardt (LM) and Newton's method. The first two are *trust region* methods whereas the last one is a *line search* method. All of the methods approximate the local behavior of the χ^2-function with a quadratic function. Newton's method does this using the first- and second-order derivatives of

the χ^2-function with respect to the LECs,

$$\chi^2(\boldsymbol{\alpha}) \approx \chi^2(\boldsymbol{\alpha}_n) + (\boldsymbol{\alpha} - \boldsymbol{\alpha}_n)^T \boldsymbol{J}_n + \frac{1}{2}(\boldsymbol{\alpha} - \boldsymbol{\alpha}_n)^T H_n (\boldsymbol{\alpha} - \boldsymbol{\alpha}_n) \tag{4.4}$$

$$J_{n,i} \equiv \left.\frac{\partial \chi^2(\boldsymbol{\alpha})}{\partial \alpha_i}\right|_{\boldsymbol{\alpha}=\boldsymbol{\alpha}_n} \tag{4.5}$$

$$H_{n,ij} \equiv \left.\frac{\partial^2 \chi^2(\boldsymbol{\alpha})}{\partial \alpha_i \partial \alpha_j}\right|_{\boldsymbol{\alpha}=\boldsymbol{\alpha}_n}. \tag{4.6}$$

If this approximation would be exact, the minimum – assuming that the Hessian H_n is positive definite so that a minimum exists – would be given by

$$\boldsymbol{\alpha}_{n+1} = \boldsymbol{\alpha}_n - \gamma_N H_n^{-1} \boldsymbol{J}_n \tag{4.7}$$

with $\gamma_N = 1$. In our non-linear problem the approximation (4.4) is not exact, therefore a line search is done by looking for a $\gamma_N \in]0, 1]$ such that $\chi^2(\boldsymbol{\alpha}_{n+1}) < \chi^2(\boldsymbol{\alpha}_n)$. If H_n is positive definite the search direction will be a descent direction making it possible to always find a suitable γ_N. In the case of negative eigenvalues, then for each negative eigenvalue λ of the Hessian we do the modification $\lambda \to -\lambda/2$ prior to the line search to make sure we move in a descent direction.

The LM minimization method also needs the Hessian H_n in every step. It obtains an approximation $\tilde{H}_n$ of H_n without second derivatives by using the fact that it is a χ^2-function that is minimized,

$$\frac{\partial^2 \chi^2(\boldsymbol{\alpha})}{\partial \alpha_i \partial \alpha_j} = \sum_{k \in \mathbb{M}} \frac{\partial^2 r_k^2}{\partial \alpha_i \partial \alpha_j} \approx \sum_{k \in \mathbb{M}} 2 \frac{\partial r_k}{\partial \alpha_i} \frac{\partial r_k}{\partial \alpha_j}. \tag{4.8}$$

The omitted term is a sum over the residuals r_k scaled with their second derivatives. Since the r_k are expected to be approximately normally distributed, with zero mean, the sum should be close to zero. Then $\boldsymbol{\alpha}_{n+1}$ is obtained using a trust-region parameter γ_{LM},

$$\boldsymbol{\alpha}_{n+1} = \boldsymbol{\alpha}_n - (\tilde{H}_n + 2\gamma_{LM} I)^{-1} \boldsymbol{J}_n. \tag{4.9}$$

This is similar to Eq. (4.7), with the most important difference being that the trust-region parameter γ_{LM} also changes the search direction to account for the limited region at which the quadratic model applies. $\gamma_{LM} = 0$ means that the quadratic model is expected to be a good approximation. For large γ_{LM} the direction will be closer to deepest descent. We have used

the implementation of the LM method provided by the GNU Scientific Library [57].

POUNDerS is a derivative-free method. It builds a quadratic approximation from several nearby χ^2-function evaluations and uses a trust region that defines where the approximation is assumed to be valid. The main benefit is that no derivative information needs to be calculated. Furthermore, noise in the χ^2-function will be smoothed out by the quadratic approximation, making the method better at avoiding small local minima than the derivative-based algorithms. See Ref. [56] for more details. POUNDerS is included in the TAO package [58] of optimization routines.

Since all of these methods are local, we need to make sure the minimum that is found is not just a local minimum. Therefore extensive searches were made in the parameter space to make sure all *feasible minima* were found. Feasible here means all minima that have a similar χ^2 value as the global minimum and obeys the physical constraints presented in Sec. 4.1. If several feasible minima are found, this indicates that more experimental data need to be included in the optimization set $\mathbb{M}$ in order to distinguish between the minima.

At LO the optimization only includes two chiral parameters, which makes it easy to find the optimal parameters. In this case it is possible to map out the χ^2-surface, in effect performing a global minimization. This is shown in Ch. 5. At NLO we start with a phase-shift minimization (see Sec. 3.3) to obtain good starting points for the minimization with scattering data. At N2LO we also do a phase-shift minimization first for the NN phase shifts. The πN sector is more well behaved so there we could start with a minimization against scattering data immediately. A optimization at N3LO would be performed in a similar fashion as for N2LO, but no such results will be presented in this work.

When we have found $\boldsymbol{\alpha}_*$ and the derivatives of $\chi^2(\boldsymbol{\alpha}_*)$ with respect to the LECs, we are in a position to determine the *statistical errors* of the observables. This will be described in the following Section.

4.4 Statistical errors

Once the parameter set $\boldsymbol{\alpha}_*$ that minimizes $\chi^2(\boldsymbol{\alpha})$ is found, we can also use the χ^2-function to construct a covariance matrix, following the derivation in Ch. 15.6 of Ref. [59]. The idea is that even though $\boldsymbol{\alpha}_*$ produces the

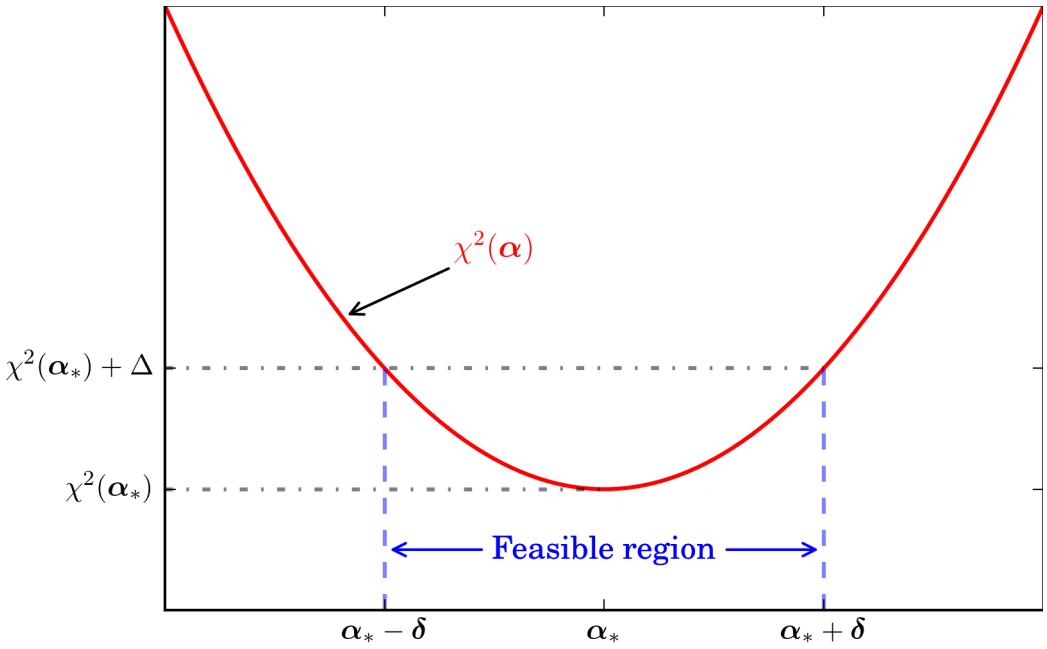

Figure 4.1: Definition of the feasible region for LECs $\boldsymbol{\alpha}_*$. Given an upper limit $\chi^2(\boldsymbol{\alpha}_*) + \Delta$ for the $\chi^2(\boldsymbol{\alpha})$ function, a feasible region *is obtained. This region (illustrated here in one dimension) defines the statistical uncertainties $\boldsymbol{\delta}$ for the LECs. See text for details.*

best fit to the data, slightly different values, $\boldsymbol{\alpha}_* + \boldsymbol{\delta}$, could also give a good description. By treating the LECs in the minimum as random variables and making the statement "good description" more rigorous, we can define statistical uncertainties in the LECs which can then be propagated to the observables.

We say that all parameter sets $\boldsymbol{\alpha}$ are *feasible* that satisfy

$$\chi^2(\boldsymbol{\alpha}) - \chi^2(\boldsymbol{\alpha}_*) \leq \Delta, \tag{4.10}$$

where Δ is some chosen tolerance, see Fig. 4.1.

Taylor expanding $\chi^2(\boldsymbol{\alpha})$ around $\boldsymbol{\alpha}_*$, where the first derivatives are zero, gives

$$\chi^2(\boldsymbol{\alpha}_* + \Delta\boldsymbol{\alpha}) - \chi^2(\boldsymbol{\alpha}_*) \approx \frac{1}{2}(\Delta\boldsymbol{\alpha})^T H(\Delta\boldsymbol{\alpha}) \tag{4.11}$$

$$H_{ij} = \left.\frac{\partial^2\chi^2(\boldsymbol{\alpha})}{\partial\alpha_i\partial\alpha_j}\right|_{\boldsymbol{\alpha}=\boldsymbol{\alpha}_*}. \tag{4.12}$$

The Hessian H is positive definite, since $\boldsymbol{\alpha}_*$ is a minimum, and it can be decomposed into $H = UDU^T$ where the columns of U are the eigenvectors of H and D is a diagonal matrix with the eigenvalues of H on the diagonal. An accurate determination of H is made possible by the use of AD (see Sec. 3.2).

Defining $\boldsymbol{x} \equiv U^T(\Delta\boldsymbol{\alpha}_*)$, Eq. (4.10) becomes

$$\frac{1}{2}\boldsymbol{x}^T D\boldsymbol{x} = \frac{1}{2}\sum_{i=1}^{N_{\boldsymbol{\alpha}}} x_i^2 D_{ii} \leq \Delta. \tag{4.13}$$

The *rotated* LEC vector $\boldsymbol{x}$ is $\boldsymbol{\alpha}$ in the eigenbasis of the Hessian. They are by construction *independent* random variables. Thus we get,

$$\frac{1}{2}x_i^2 D_{ii} \leq \Delta_1 \tag{4.14}$$

where Δ_1 is the limit to use when considering only variations in one parameter and keeping the others fixed. If $\chi^2(\boldsymbol{\alpha})$ would follow a chi-squared distribution around the minimum, then $x_i^2 D_{ii}/2$ will follow a chi-squared distribution with one degree of freedom, meaning that a 1σ confidence level is given by $\Delta_1 = 1$, and $x_i \sim \mathcal{N}(0, 2/D_{ii})$. In practice, $\chi^2(\boldsymbol{\alpha})$ will not exactly be a chi-squared distribution. This will affect what value should be used for Δ_1. The only correction we do is to normalize $\chi^2(\boldsymbol{\alpha})$ so that $\chi^2(\boldsymbol{\alpha}_*) = N_{\text{dof}}$, leading to $\Delta_1 = \chi^2(\boldsymbol{\alpha}_*)/N_{\text{dof}}$. We assume normally distributed parameters as an approximation. This results in the covariance matrix

$$C = 2\frac{\chi^2(\boldsymbol{\alpha}_*)}{N_{\text{dof}}} H^{-1} \tag{4.15}$$

Since Δ_1 only affects C with a constant factor, correlations are unaffected by the choice of Δ_1, as long as the Taylor expansion of $\chi^2(\boldsymbol{\alpha})$ is valid.

The statistical uncertainties of the LECs are presented as $\sigma_{\alpha_i} = \sqrt{C_{ii}}$. However, since the LECs are correlated, they can not be varied independently. The uncertainty σ_{α_i} is the *maximal variation*, within one standard deviation, allowed by LEC i assuming all other LECs are varied simultaneously so as to minimize the χ^2 value.

4.5 Propagated statistical errors

With the covariance matrix C we can propagate statistical errors to observables and calculate correlations of observables and LECs. The

covariance matrix for the LECs defines the probability distribution of LEC values. From this a probability distribution for observables can be obtained, from which statistical errors and correlations can be extracted. The dependence of the observables on the LECs are usually approximated by a Taylor expansion around the minimum $\boldsymbol{\alpha}_*$, which will allow for analytical results. To calculate the covariance of two observables $O_a^{(\text{theo})}(\boldsymbol{\alpha})$ and $O_b^{(\text{theo})}(\boldsymbol{\alpha})$ it is most convenient to use the independent parameters $\boldsymbol{x}$ defined above, where each x_i is normally distributed with zero mean.

Using a Taylor expansion to second order, and denoting the Jacobian and Hessian with respect to the LECs, $\boldsymbol{J}_a$ and H_a respectively, we get

$$\begin{aligned} O_a^{(\text{theo})}(\boldsymbol{\alpha}_* + \Delta\boldsymbol{\alpha}) &\approx O_a^{(\text{theo})}(\boldsymbol{\alpha}_*) + (\Delta\boldsymbol{\alpha})^T \boldsymbol{J}_a + \frac{1}{2}(\Delta\boldsymbol{\alpha})^T H_a (\Delta\boldsymbol{\alpha}) \\ &= O_a^{(\text{theo})}(\boldsymbol{\alpha}_*) + \boldsymbol{x}^T U^T \boldsymbol{J}_a + \frac{1}{2}\boldsymbol{x}^T U^T H_a U \boldsymbol{x} \\ &\equiv O_a^{(\text{theo})}(\boldsymbol{\alpha}_*) + \boldsymbol{x}^T \tilde{\boldsymbol{J}}_a + \frac{1}{2}\boldsymbol{x}^T \tilde{H}_a \boldsymbol{x} \end{aligned} \tag{4.16}$$

$$\begin{aligned} \mathbb{E}[O_a^{(\text{theo})}(\boldsymbol{\alpha}_* + \Delta\boldsymbol{\alpha})] &\approx O_a^{(\text{theo})}(\boldsymbol{\alpha}_*) + \frac{1}{2}\sum_{ij} \tilde{H}_{a,ij}\mathbb{E}[x_i x_j] \\ &= O_a^{(\text{theo})}(\boldsymbol{\alpha}_*) + \frac{1}{2}\sum_{i} \tilde{H}_{a,ii}\sigma_{x_i}^2 \end{aligned} \tag{4.17}$$

where $C = U\Sigma U^T$ is the eigenvalue decomposition of the covariance matrix with eigenvalues $\Sigma_{ii} \equiv \sigma_{x_i}^2$. $\tilde{H}_a$ and $\tilde{J}_a$ are the rotated Hessian and Jacobian respectively. The calculation of the covariance between two observables is then straight forward,

$$\begin{aligned} \sigma_{ab} &\equiv \mathbb{E}[(O_a^{(\text{theo})}(\boldsymbol{\alpha}) - \mathbb{E}[O_a^{(\text{theo})}(\boldsymbol{\alpha})])(O_b^{(\text{theo})}(\boldsymbol{\alpha}) - \mathbb{E}[O_b^{(\text{theo})}(\boldsymbol{\alpha})])] \\ &\approx \tilde{J}_a^T \Sigma \tilde{J}_b + \frac{1}{2}(\boldsymbol{\sigma}^2)^T (\tilde{H}_a \circ \tilde{H}_b)\boldsymbol{\sigma}^2, \end{aligned} \tag{4.18}$$

where $\boldsymbol{\sigma}^2$ is the diagonal of Σ. Using a linear approximation is equal to setting $H_a = H_b = 0$. The variance σ_a^2 of an observable is obtained by setting $a = b$.

The linear approximation will result in the familiar Gaussian probability distribution for the observables, since that is the probability distribution of the LECs. This is not the case for the quadratic approximation. Although there is still an analytical expression for the covariance (Eq. (4.18)) in this case, no analytical expression for the probability distribution is known to us. Therefore, this is approximated by sampling N_q LEC parameter vectors from

the probability distribution of the LECs, which is given by the multivariate normal distribution. These LEC vectors are then used to calculate the observable value according to Eq. (4.16), which then results in the desired probability distribution. N_q can be chosen very large since no full calculation of the observables is involved, making the obtained probability distributions very exact.

To test the validity of the quadratic approximation (4.16) of the observables, the obtained probability distributions can be compared to a Monte Carlo simulation. Here the observable value is recalculated using the appropriate methods presented in Ch. 3 for N_{mc} sets of LECs to obtain a probability distribution. Such a comparison will be presented in the next Chapter.

4.6 Correlations

The *correlation* between two LECs or observables a and b is defined as $c_{ab} = \sigma_{ab}/(\sigma_a\sigma_b)$. The correlation can have values between -1 and 1. A value of zero means that a and b are uncorrelated, while -1 and 1 means fully anti correlated and fully correlated, respectively. Note that this measures the *linear correlation*. Therefore, it is most suitable when the observables depend linearly on the LECs. This is the case if the statistical uncertainties are small. As an example, probability distributions for two LECs with different amount of correlation are shown in Fig. 4.2.

Correlations between LECs arise when observables in the objective function depend strongly on several LECs, which is usually the case. For example, assume we add a fictitious observable O_f to our objective function, with $O_f^{(\mathrm{expr})} = 0$, $O_f^{(\mathrm{theo})}(\boldsymbol{\alpha}) = a - b$ and uncertainty $\sigma_{f,\mathrm{total}}$. This will result in a term $((a-b)/\sigma_{f,\mathrm{total}})^2$ in the objective function. Assuming that a and b were previously uncorrelated ($c = 0$) the inclusion of O_f will not reduce the uncertainty in LECs a and b. It does, however, increase the correlation, with smaller $\sigma_{f,\mathrm{total}}$ corresponding to larger c_{ab}. If we instead define the *rotated* LECs $x \equiv a - b$ and $y \equiv a + b$ we see that x will be constrained by O_f. Thus, in this case, the linear combinations x and y more clearly shows what directions in the LEC parameter space that are constrained by the objective function. This is precisely the advantage of looking at the rotated and uncorrelated LEC vector $\boldsymbol{x}$ defined in Sec. 4.4. If the inclusion of O_f results in the direction x being well constrained, then the ideal observable

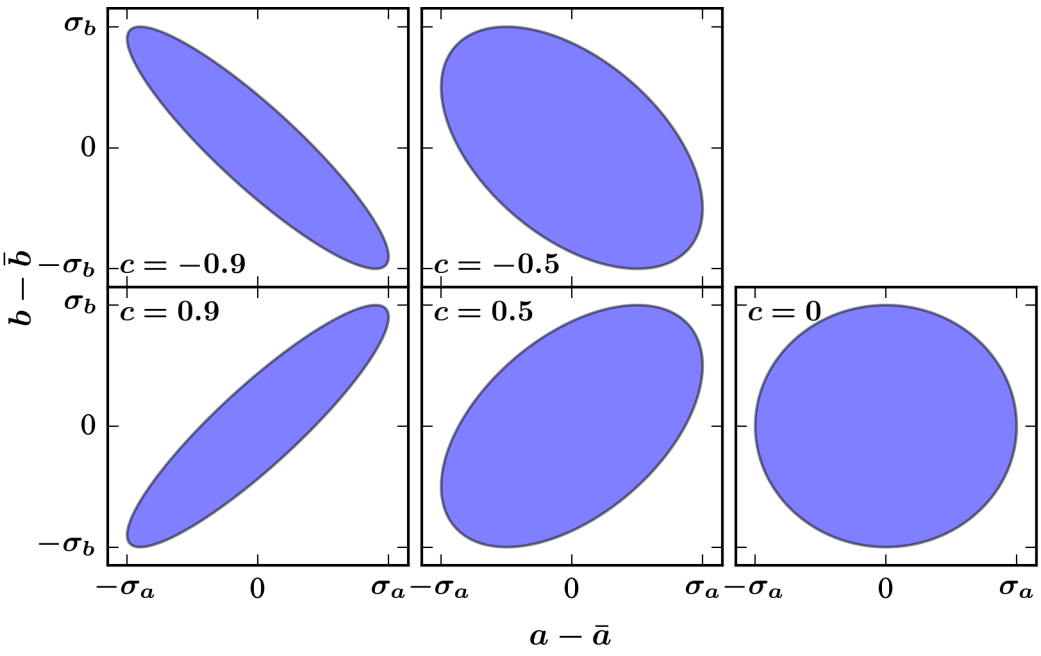

Figure 4.2: 1σ *contours for two (centered) LECs* a *and* b *assuming different values of the correlation coefficient* $c_{ab} = c$*. The correlation measures how much the values of the LECs depend on each other. E.g. for the case* $c = 0.9$ *an increase in the value of* a *will highly increase the probability that* b *have a larger value too. Note that the* 1σ*-level for a single LEC always corresponds to the most extreme values of the contour. This means that strong correlations does not affect the uncertainties of the LECs but it affects the size of the feasible LEC parameter space.*

O_g to include in addition, to maximally constrain the model, would depend on the LECs like $O_g^{(\mathrm{theo})}(\boldsymbol{\alpha}) \sim a + b$, as this is orthogonal to O_f.

This analysis can give guidance in finding suitable observables needed to constrain the interaction further. If two LECs are heavily correlated, then an observable which anti correlates those LECs is ideally needed to constrain the model better. Alternatively, the correlations between observables can be used directly to see which observables can be used to decrease the statistical uncertainty of other observables.

Note that the statistical uncertainty from the fitting is only part of the uncertainty of the resulting predictions. However, if the statistical uncertainties can be shown to be small, discrepancies between theory and experiment will depend on systematical model errors. This makes it easier to analyze the model uncertainties.

Chapter 5

Results

With the model and the methods described in Chs. 2 and 3 we have a complete theory for a low-energy nuclear interaction. In Ch. 4 we showed how such an interaction is constructed using mathematical optimization routines. In this Chapter we will describe how the model is used and what physics results have been obtained.

We will mainly discuss the results presented in Paper 2. Paper 1 is similar in spirit to Paper 2, with the goal of quantifying the uncertainties in χEFT predictions. The main difference is that we in Paper 2 have made full use of the tools presented in detail in this Thesis.

This Chapter is structured as follows. We will begin by discussing the choice of objective function $\chi^2(\boldsymbol{\alpha})$ in Sec. 5.1. The minimization and some practical issues related to this are presented in Sec. 5.2. Finally, the resulting predictions from the obtained potentials are shown in Sec. 5.3.

5.1 The objective function

The first step towards obtaining results is defining an objective function. That is, choosing what observables that go into the $\chi^2(\boldsymbol{\alpha})$-function. The goal with the model is to be able to make predictions of observables that are hard to measure experimentally, or that have not yet been measured. As much known data should be included in the objective function as possible to obtain the most accurate and precise results. If a good fit to all available data is possible, this strategy should produce the least uncertainty in the unknown observables.

The studies in Paper 1 and 2 are only investigative. This means that we include a subset of the known data, to see if we can reproduce other known data that is not included in the objective function. This is a good way to test the validity of the model and the methods.

There is another reason to sometimes exclude known data, related to uncertainty estimation. A set of K different objective functions can be chosen that have slightly different, but overlapping, datasets. The datasets should still be chosen such that the model is well enough constrained. For each objective function a set of LECs will be obtained from the fitting. The corresponding potentials will produce slightly different predictions. This difference can then be used to gauge the model uncertainty. See Ref. [55] for more details. In Sec. 5.3.4 we use different objective functions to estimate the model uncertainty of bound state properties at N2LO.

In Paper 1 we looked only at the NN part of the N2LO interaction and used NN scattering data up to 125 MeV in the objective function. In Paper 2, we used all the tools described in this Thesis. Therefore, when fitting the N2LO potential we could include all πN scattering data form the WI08 database up to 70 MeV, all NN scattering data from the SM99 database up to 290 MeV, and bound-state properties for $A = 2, 3$ nuclei. We also included the 3N interaction.

In Paper 2 we also performed optimizations at LO and NLO in order to gauge the order-by-order convergence. For these potentials we did not use any πN or $A = 3$ observables. The πN data was excluded since there are no LECs at orders below N2LO that connect the πN-interaction with the NN interaction. The 3N data was excluded since there is no 3N force below N2LO. The 3N data could in principle be included anyway, we would only expect a larger model error for LO and NLO compared to N2LO. However, since we have no good estimation of the model error for bound-state properties, the inclusion of the 3N data could negatively affect the fitting procedure. At NLO we include the nn ERE parameters a_{nn}^{N} and r_{nn}^{N} in order to have some data constraining the LEC $\tilde{C}_{^1S_0}^{(\text{nn})}$.

In Paper 2 we looked at two different set of potentials where we used two different minimization schemes. In this Thesis we will only focus on the *simultaneously optimized* potentials from Paper 2, called LOsim, NLOsim and NNLOsim.

With the objective function defined, we need to fit the LECs by minimizing the objective function value.

5.2 Minimization of the χ^2-function

Due to the iterative process of determining the model error scaling constants C_{NN} and $C_{\pi\text{N}}$, described in Sec. 2.4, the minimization of the χ^2-function is a multi-step process. The model error constants are chosen such that $\chi^2_{(\text{x})}/N^{(\text{x})}_{\text{dof}} = 1$ where x stands for NN and πN. Since the scattering data is the bulk of the observables included in the objective function, the final χ^2/N_{dof} will always be close to 1 in the minimum.

The minimization of the χ^2-function is greatly aided by having access to the first- and second-order derivatives calculated using AD. However, there is still a risk of finding an erroneous local minimum. At LO there are only two parameters to fit, making it easy to find the global minimum. In that case, with the objective function consisting of NN scattering data and deuteron properties, it was seen that only one minimum exists, shown in Fig. 5.1(a). For this simple case it is instructive to take a closer look at the χ^2-function.

If we exclude the deuteron properties from the χ^2-function, an extra local minimum appears, which is clearly worse than the global optimum, see Fig. 5.1(b). The two minima differ mainly in the value of $\tilde{C}_{^3S_1}$ and the depth of the minima. The χ^2/N_{dof} for the global and shallow minima is 1.0 and 3.0, respectively. The two LECs are expected to have roughly the same value due to the approximate Wigner SU(4) symmetry described in Sec. 4.1, which favors the global minimum. Although the shallow minimum can also be immediately discarded due to its large χ^2/N_{dof} value, several minima is a sign that we have not constrained the model sufficiently. In this case, the inclusion of the deuteron properties provides the needed constraints.

The deuteron is a bound state in the coupled ${}^3S_1 - {}^3D_1$ channel. This means that the only LEC affecting the deuteron at LO is $\tilde{C}_{^3S_1}$, precisely the LEC that differs in value for the two minima. Due to the very small error bar on the deuteron binding energy (see Tab. 3.2) the inclusion of the deuteron properties in the objective function puts a very tight constraint on $\tilde{C}_{^3S_1}$. This tight constraint is aligned almost perfectly with the previously obtained global minimum. Thus, the values of the LECs for the LOsim potential (see Fig. 5.1(a)) where the deuteron properties are included, match (within the statistical uncertainties) with the ones in the global minimum shown in Fig. 5.1(b).

To conclude, the inclusion of the deuteron properties removed the unwanted local minimum and, at the same time, did not worsen the description of the already included scattering data.

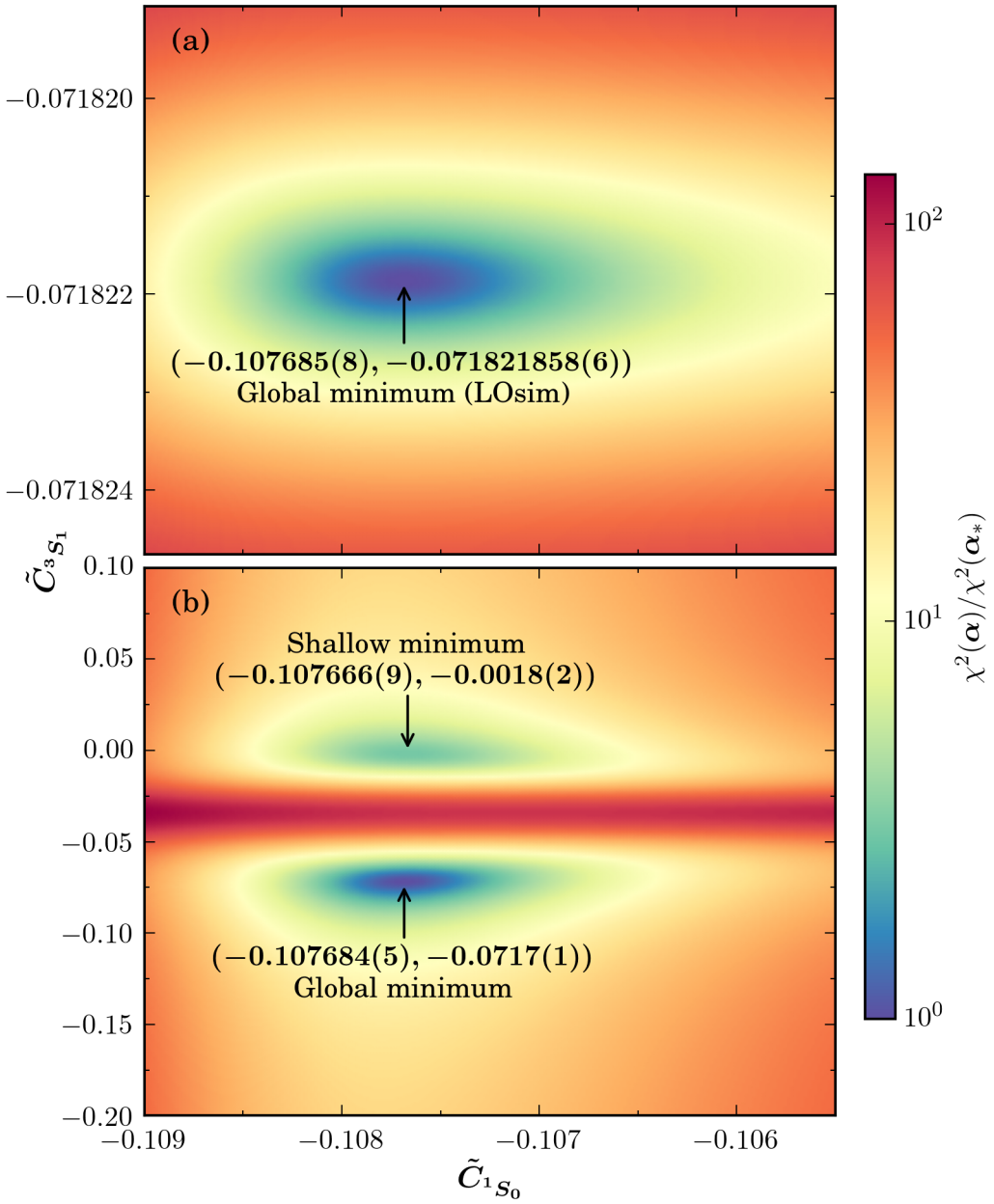

Figure 5.1: $\chi^2(\tilde{C}_{^1S_0}, \tilde{C}_{^3S_1})$ *surface for the LO minimization when including scattering data up to* 290 MeV *and the deuteron properties (panel (a)). When excluding the deuteron properties, an extra, shallow, minimum appears, shown in panel (b). The uncertainties of the LECs shown in the figure are the statistical uncertainties. The* $\tilde{C}_x$ *are in units of* $10^4\,\mathrm{GeV}^{-2}$.

At NLO, with 11 LECs, it gets more complicated. There are several NN contact LECs affecting the same partial-wave, implying parameter correlations. At NLO there are two (three) LECs affecting the ${}^1S_0$ (${}^3S_1 - {}^3D_1$) channel. As stated in Sec. 4.3, we begin with a phase shift minimization to find suitable starting points. The main benefit of this is that each partial wave is fitted separately. At this stage we find two minima in the ${}^1S_0$ channel and two minima in the ${}^3S_1 - {}^3D_1$ channel. The combination of these result in a total of *four different minima*. When performing the full fitting to data using the χ^2-function, we find four corresponding minima. Note that we here include both the NN scattering data and the deuteron properties, meaning that the deuteron properties are not enough at NLO to remove all but one minimum. It is not surprising that the NLO potential, with more operator structures than the LO potential, needs more experimental data to be properly constrained.

It is interesting to note that all of the minima result in almost identical predictions for all included $A = 2$ observables, see Tab. 5.1. This implies that we cannot immediately discard any of the minima due to a large χ^2/N_{dof} value as in the LO case. However, due to the approximate Wigner SU(4) symmetry, the two LO NN contact LECs should still be of roughly the same size. Therefore, the minima NLO-2 and NLO-3 can be discarded. We are not able to distinguish between the two remaining minima using only the $A = 2$ data. We need to either look at the $A = 3$ observables or compare with the LEC values obtained in the N2LO potential. Had we included the $A = 3$ observables in the NLO minimization, minimum 4 would stand out, as can be seen in Tab. 5.1. Comparing the LEC values with the ones for N2LOsim provides a confirmation that minimum 4 seems to be the correct one, as we do not expect the values of the LECs to change too much between orders. For these reasons, it is the minimum NLO-4 that defines the potential NLOsim. For a more thorough discussion, see Paper 2.

At N2LO there are 15 additional LECs to fit, adding up to a total of 26 parameters. This increases the risk of finding spurious local minima. However, since we also include the πN and $A = 3$ observables we have enough diversity in the data to eliminate all spurious minima. We are left with one minimum that defines the N2LOsim potential. This once again shows the importance of including all this data in the objective function and performing a simultaneous fit.

The obtained LEC values together with their statistical uncertainties are presented in Tabs. 5.2 and 5.3. The NN LECs are in general of natural

Table 5.1: Comparison of the different NLO minima obtained after fitting the LECs to NN scattering data up to 290 MeV *and the deuteron properties. The minima produces almost identical predictions for* $A = 2$ *observables, but can be seen to differ for* $A = 3$ *observables. The* $\tilde{C}$ *LECs are in units of* $10^4\,\mathrm{GeV}^{-2}$*. The scattering* χ^2/N_{dof} *shown are for data up to* 125 MeV *without model errors included.* $E^{(exp)}(^3H) \approx -8.48\,\mathrm{MeV}$

	$\tilde{C}^{(\mathrm{np})}_{^1S_0}$	$\tilde{C}_{^3S_1}$	χ^2/N_{dof}	$E(^2\mathrm{H})(\mathrm{MeV})$	$E(^3\mathrm{H})(\mathrm{MeV})$
NLO-1	+0.81	+0.68	14	−2.22	−3.08
NLO-2	+0.81	−0.17	14	−2.22	−3.39
NLO-3	−0.15	+0.68	14	−2.22	−2.97
NLO-4	−0.15	−0.18	14	−2.22	−8.27
N2LOsim	−0.15	−0.17	1.7	−2.22	−8.54[a]

[a] Here calculated without including a 3N force.

size. Most statistical uncertainties are on the order of a few percent. At LO the LECs have very small statistical uncertainties. The reason for this is that there will be very little correlation between the two parameters that exist at this order. The tight constraint on the deuteron binding energy will then directly translate to a constraint on $\tilde{C}_{^3S_1}$. At NLO (N2LO) there are three (six) LECs affecting the deuteron. Therefore, the tight constraint on the deuteron energy will result in increased correlations among these LECs instead of very small uncertainties, see Sec. 4.6.

The πN LECs, however, have much larger uncertainties and some are unnaturally large. Especially the πN LECs that only affect the πN data have large uncertainties. The e_x LECs are very poorly constrained by the data. This suggests that more diverse and more accurate πN scattering data would be needed to further constrain this part of χEFT.

As stated in Sec. 4.2, we expect the distribution of the residuals,

$$\frac{O_k^{(\mathrm{theo})}(\boldsymbol{\alpha}_*) - O_k^{(\mathrm{expr})}}{\sigma_{k,\mathrm{total}}},$$

to approximately follow a normal distribution. This distribution of residuals is shown in Fig. 5.2 for the N2LO potential. It is clearly not a perfect normal distribution. The deviations are mainly due to the systematical model error. If a systematical error dominates, many residuals will be either positive or

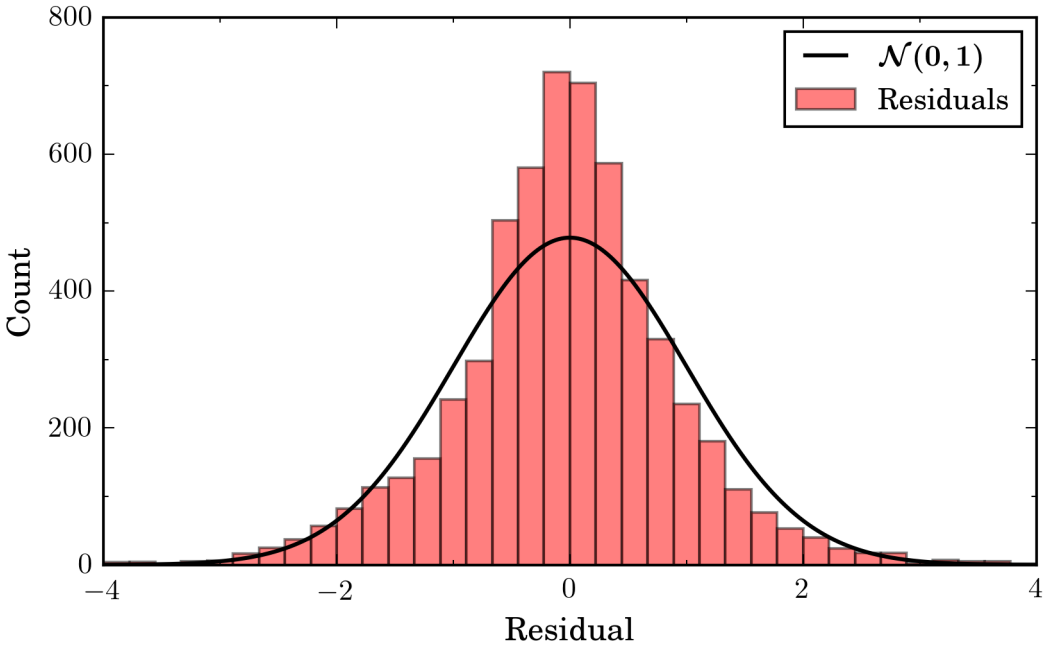

Figure 5.2: The distribution of residuals in the χ^2-function for the N2LOsim potential. The residuals should be approximately normally distributed. There are clear deviations from normality, which is due to the systematical model uncertainty. (From Paper 2)

negative. This will cause a nonzero skewness in the distribution, which can be seen in the Figure. Furthermore, if our assumed momentum dependence is not entirely correct, the approximated model error might overestimate the uncertainty in some momentum intervals and underestimate it in others. This will cause a too sharp peak in the residual distribution. This is seen in Fig. 5.2 and indicates that the model error would need some refining in order for the residual distribution to be like a normal distribution.

To make sure that it is only the model error that cause deviations from normality we can look at a subset of the residuals where the model error is expected to be small. When we optimize the N2LO potential using instead a maximum T_{lab} of 125 MeV for the NN scattering data, and considering only the NN scattering residuals, there is no skewness and only a small excess peak.

The *correlation matrix* for some of the LECs in the N2LOsim potential is shown in Fig. 5.3. It is clear that most of the LECs are strongly correlated

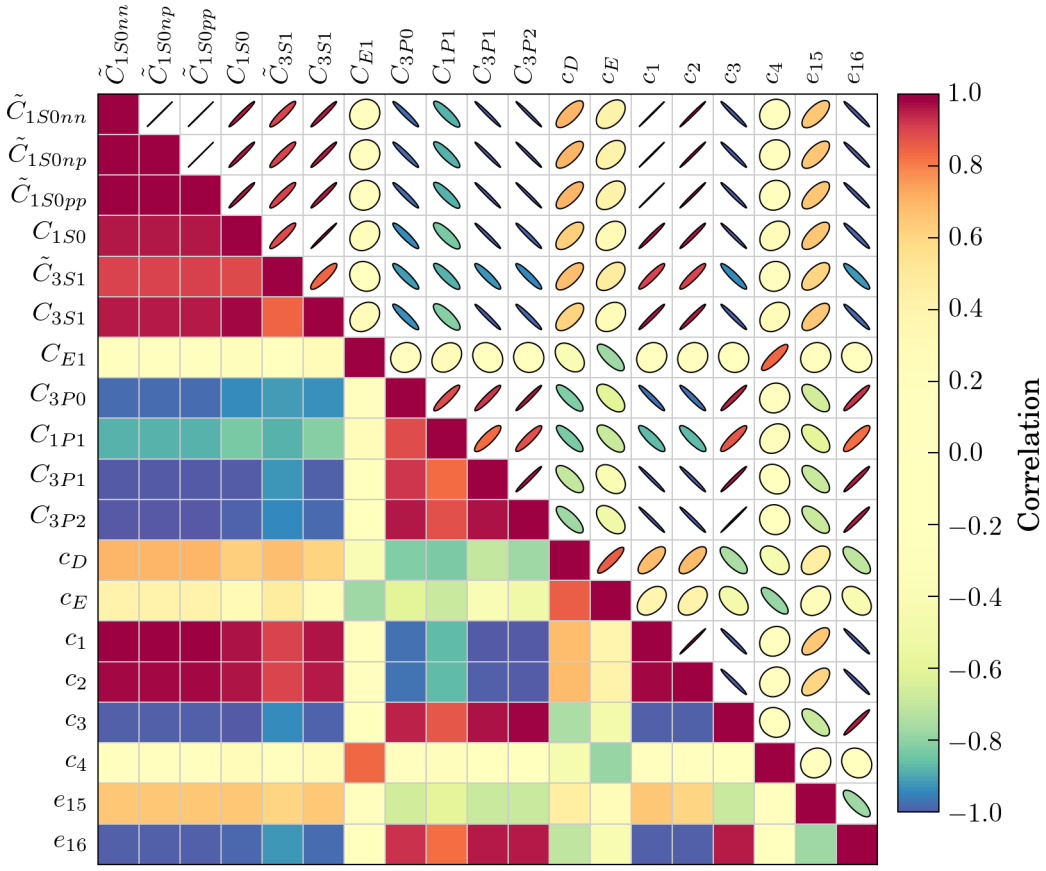

Figure 5.3: Correlation ellipses for some of the LECs in the N2LOsim potential. There are many strong correlations between the LECs indicating that the LECs can not be varied independently. (From paper 2)

with each other. As was discussed already in Sec. 4.6, this is a result of many observables depending simultaneously on several LECs. This means that a change in one LEC must be accompanied with corresponding changes in all other LECs to keep the χ^2-value low.

Now that we have discussed the minimization, the resulting LEC values and their properties, it is finally time to proceed to the ultimate goal: predictions for observables with corresponding uncertainties.

Table 5.2: NN and 3N LEC values for the simultaneously optimized LO, NLO and N2LO potentials presented in Paper 2. The values relative to their natural sizes (see Eq. (4.1)) are in the fourth column. The last column is the uncertainty relative to the natural size of the LEC. The values of the $\tilde{C}_x$ are in units of $10^4\,\mathrm{GeV}^{-2}$, the C_x in units of $10^4\,\mathrm{GeV}^{-4}$ and c_D and c_E are dimensionless.

	LEC	Value	Rel. magnitude	Rel. uncertainty
LO	$\tilde{C}_{^1S_0}$	−0.1076846(80)	0.73	0.0054%
LO	$\tilde{C}_{^3S_1}$	−0.0718218580(56)	0.49	3.8×10^{-6}%
NLO	$\tilde{C}^{(\mathrm{np})}_{^1S_0}$	−0.150623(79)	1.0	0.054%
NLO	$\tilde{C}^{(\mathrm{pp})}_{^1S_0}$	−0.14891(11)	1.0	0.075%
NLO	$\tilde{C}^{(\mathrm{nn})}_{^1S_0}$	−0.14991(27)	1.0	0.18%
NLO	$C_{^1S_0}$	+1.6935(83)	2.9	1.4%
NLO	$\tilde{C}_{^3S_1}$	−0.1843(16)	1.3	1.1%
NLO	$C_{^3S_1}$	−0.218(14)	0.37	2.4%
NLO	$C_{^3S_1-{}^3D_1}$	+0.264(16)	0.45	2.7%
NLO	$C_{^3P_0}$	+1.2998(85)	2.2	1.4%
NLO	$C_{^1P_1}$	+1.025(59)	1.7	10%
NLO	$C_{^3P_1}$	−0.336(10)	0.57	1.7%
NLO	$C_{^3P_2}$	−0.2029(15)	0.34	0.26%
N2LO	$\tilde{C}^{(\mathrm{np})}_{^1S_0}$	−0.1474(20)	1.0	1.3%
N2LO	$\tilde{C}^{(\mathrm{pp})}_{^1S_0}$	−0.1465(20)	1.0	1.3%
N2LO	$\tilde{C}^{(\mathrm{nn})}_{^1S_0}$	−0.1471(20)	1.0	1.3%
N2LO	$C_{^1S_0}$	+2.548(47)	4.3	7.9%
N2LO	$\tilde{C}_{^3S_1}$	−0.1687(21)	1.1	1.5%
N2LO	$C_{^3S_1}$	+0.705(47)	1.2	8.0%
N2LO	$C_{^3S_1-{}^3D_1}$	+0.597(11)	1.0	1.9%
N2LO	$C_{^3P_0}$	+1.160(30)	2.0	5.2%
N2LO	$C_{^1P_1}$	+0.520(33)	0.88	5.6%
N2LO	$C_{^3P_1}$	−0.955(31)	1.6	5.2%
N2LO	$C_{^3P_2}$	−0.658(30)	1.1	5.1%
N2LO	c_D	−0.324(51)	0.32	5.1%
N2LO	c_E	−0.521(15)	0.52	1.5%

Table 5.3: πN LECs for the simultaneously optimized N2LO potential presented in Paper 2. For notation, see Tab. 5.2. The c_x, d_x and e_x LECs are given in units of GeV^{-1}, GeV^{-2} and GeV^{-3}, respectively.

	LEC	Value	Rel. magnitude	Rel. uncertainty
N2LO	c_1	+0.22(29)	0.42	55%
N2LO	c_2	+5.1(10)	9.7	200%
N2LO	c_3	−3.56(13)	6.7	25%
N2LO	c_4	+3.933(85)	7.4	16%
N2LO	$d_1 + d_2$	+5.320(94)	19	33%
N2LO	d_3	−4.83(22)	17	79%
N2LO	d_5	−0.24(14)	0.83	49%
N2LO	$d_{14} - d_{15}$	−10.23(27)	36	95%
N2LO	e_{14}	−0.26(89)	1.7	590%
N2LO	e_{15}	−9.3(24)	61	1600%
N2LO	e_{16}	−0.0(41)	0.21	2700%
N2LO	e_{17}	+1.5(18)	9.9	1200%
N2LO	e_{18}	−1.2(16)	7.6	1100%

5.3 Predictions with uncertainties

With optimized potentials at the orders LO, NLO and N2LO we will demonstrate some results to see the quality of the potentials. See Paper 2 for additional discussions and Paper 1 for a preliminary study.

5.3.1 Scattering data

Due to the large amount of scattering data in the databases, we do not show a comparison between theory and experiment for each data point. Instead, we show the overall quality of the potentials for different scattering energy intervals and also some selected scattering data.

The overall quality of the fit to NN scattering data is shown using partial χ^2-values, $\chi^2_T/N^{(T)}_{\text{dof}}$, where T is the maximum T_{lab}. That is, each partial χ^2-value includes NN scattering data up to lab-scattering energy T. In determining the size of the NN scattering model error, we required that $\chi^2_{290}/N^{(290)}_{\text{dof}} = 1$. The $\chi^2_T/N^{(T)}_{\text{dof}}$ for some values of T are shown in Fig. 5.4(a) for the NN scattering. If our approximation of the model error was correct, we would expect the curve to have a value around 1 for all T. However, the curve displays some deviations from unity, which indicates that the approximation for the model error may be too crude.

Due to the normalization to 1 at the highest energy, Fig. 5.4(a) does not say anything about the size of the model error itself. To get a clearer picture of how well the potentials describe the NN scattering data, Fig. 5.4(b) shows instead the partial χ^2-values without the model error included. The NN scattering data description is significantly improved from order to order. The low-energy data is described most accurately by the potentials, which is to be expected since χEFT is a low-energy model.

The πN scattering data without the model error included is shown in Fig. 5.4(c). Here the description is not better for lower energies, as not even the lowest included data is accurately described.

Some example scattering data with model uncertainties are shown in Fig. 5.5. The total and differential cross sections shown in Figs. 5.5(a,b) displays a trend of increasing accuracy and decreasing model errors as the order increases. Some πN scattering data is shown in Figs. 5.5(c,d).

The statistical uncertainties of the theoretical values turned out to be much smaller than the model error for the scattering data. Therefore, we have only shown the model errors in Fig. 5.5.

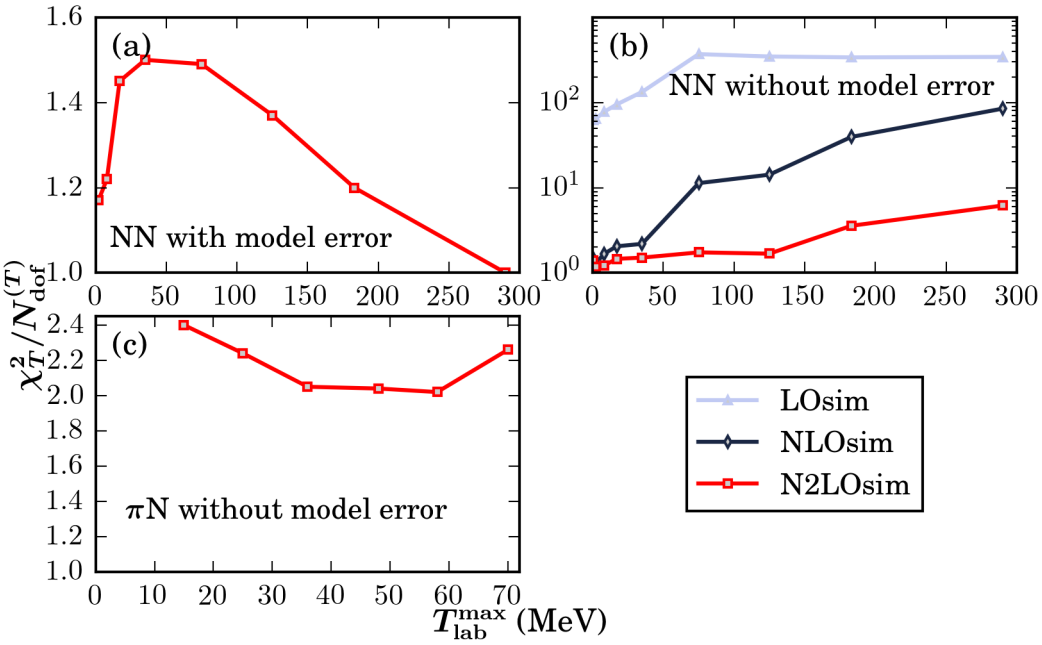

Figure 5.4: Partial χ^2-values for scattering data. $\chi^2_T/N^{(T)}_{\rm dof}$ is defined as the partial χ^2-value involving only scattering data up to lab-scattering energy T for either NN or πN data. (a) NN scattering including the model error, which is normalized to 1 *at* $T_{\rm lab} = 290\,$MeV. *(b) NN scattering without the model error. A clear convergence when increasing the chiral order is seen. Also an improved description as the energy decreases. (c) πN scattering without the model error. Here the model does not provide a better description of the data for the lower energies. (From Paper 2)*

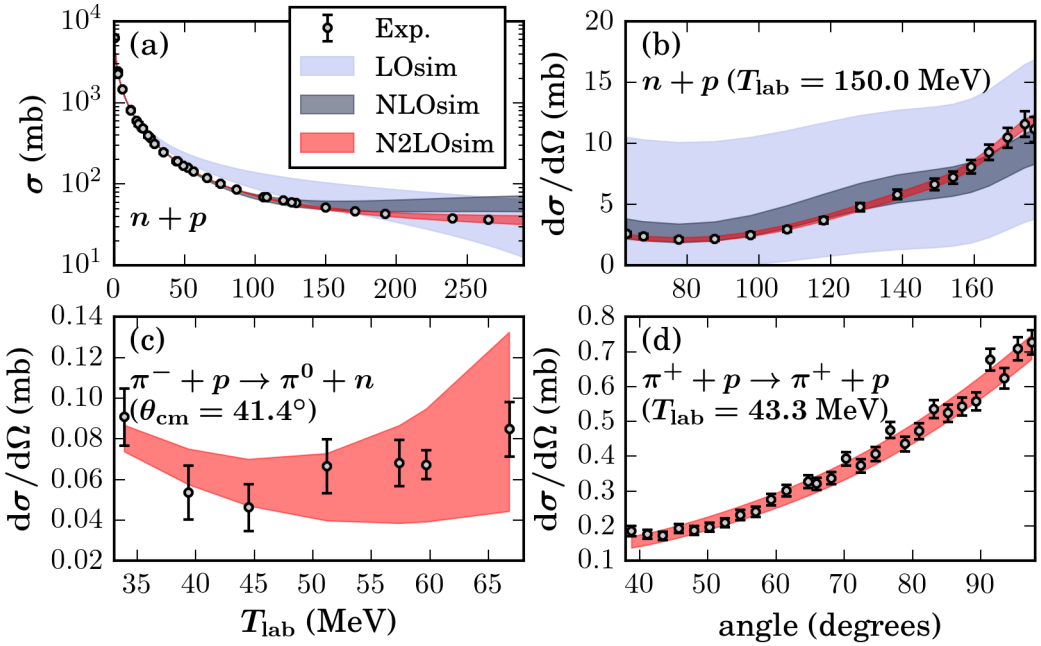

Figure 5.5: Some example NN and πN scattering data. The colored bands show the model errors. Panel (a) shows the total cross section for np scattering while panels (b) to (d) show differential cross sections. (From Paper 2)

5.3.2 Bound-state properties and ERE parameters

Apart from the scattering observables we have also computed bound-state properties and ERE parameters. The obtained values for the LOsim, NLOsim and N2LOsim potentials are presented in Tab. 5.4. The uncertainties on the theoretical values are statistical uncertainties calculated using the quadratic approximation described in Sec. 4.5. All values are shown with four digits of precision.

As expected, the statistical uncertainties are small for LOsim since only two LECs were fitted. For NLOsim and N2LOsim the statistical uncertainties are comparable, although a bit smaller for N2LOsim in general. The asymmetrical errors are due to the nonlinear dependence of the observables on the LECs.

A set of observables are predictions for all potentials. These are: $E(^4\text{He})$, $r_{\text{pt-p}}(^4\text{He})$ and the ERE parameters for the np and pp systems. All of these observables show a converging trend towards the experimental value as the chiral order increases. For the ^{4}He properties the statistical uncertainties are large enough at N2LO to explain the deviation from the experimental values. This suggests that the model error is not larger than the statistical uncertainty in this case. However, in Sec. 5.3.4 we will see that the model error seems to be much larger than the statistical uncertainty. For the ERE parameters there are some discrepancies at all orders, in particular for the precise pp ERE parameters.

The deuteron radius, $r_{\text{pt-p}}(^2\text{H})$, is also interesting. It is the only non-scattering observable included in the objective function that is not correct within one standard deviation of the combined experimental and method uncertainty. The discrepancy is even worse at N2LO than at NLO. One explanation to this could be that the correction term Δr^2 in Eq. (3.34) is in fact not negligible. The contributions entering Δr^2 have been estimated to be of the size $0.013\,\text{fm}^2$ in Ref. [60] and $0.016\,\text{fm}^2$ in Ref. [61], which could explain some of the discrepancy.

5.3.3 Statistical error propagation

As mentioned in Sec. 4.5 we can compare our approximate statistical uncertainties with a Monte Carlo sampling. Such a comparison is presented in Fig. 5.6, where the joint probability distribution for $E(^4\text{He})$ and $r_{\text{pt-p}}(^2\text{H})$ is shown. The number of Monte Carlo samples used was $M_{mc} = 10^5$. The

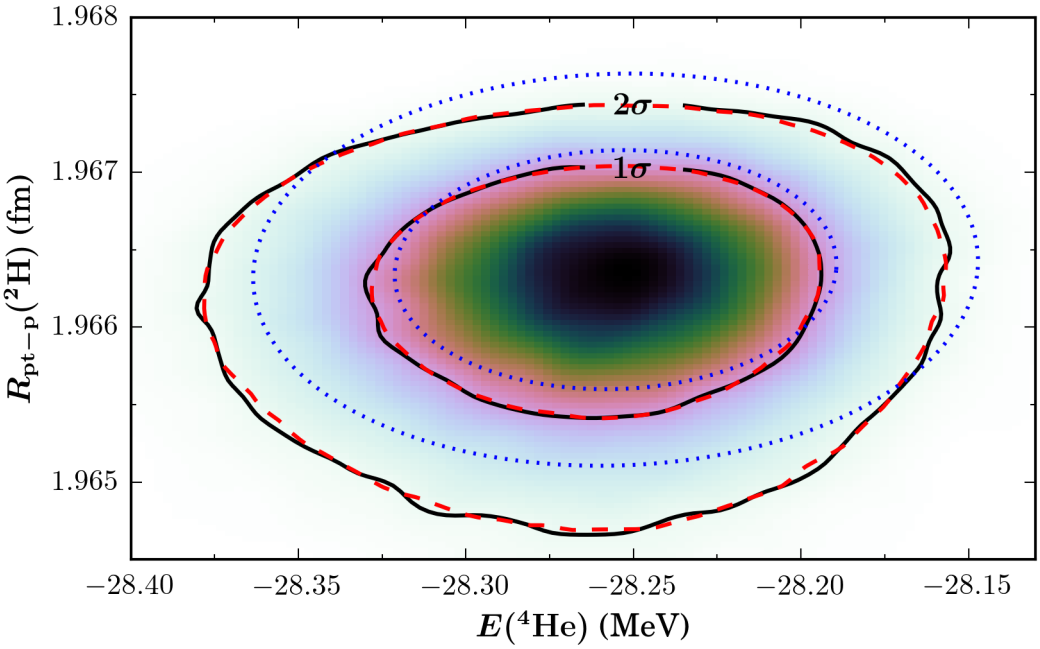

Figure 5.6: Joint probability distribution for $E(^4He)$ and $r_{pt\text{-}p}(^2H)$ for the N2LOsim potential obtained using Monte Carlo sampling. Contours are shown using black, solid lines. Contours for the distributions obtained assuming a linear (quadratic) dependence on the LECs are shown with blue dotted (red dashed) lines. (From Paper 2)

contour lines for the distributions obtained using Monte Carlo sampling and the quadratic approximation described in Sec. 4.5 align perfectly. However, the linear approximation is seen to deviate somewhat. In the same figure we see that the correlation coefficient c for these observables is rather small, with a calculated value of $c = 0.06$.

5.3.4 Estimation of model uncertainties

For some final results we will look at an alternative estimation of the model error. The idea, briefly mentioned in Sec. 5.1, is to construct several similar potentials using slightly different objective functions.

With this aim, we performed six different optimizations at N2LO. The same experimental data was used in the objective function as in N2LOsim, except that the upper limit $T_{\mathrm{lab}}^{\mathrm{max}}$ for the included NN scattering data was

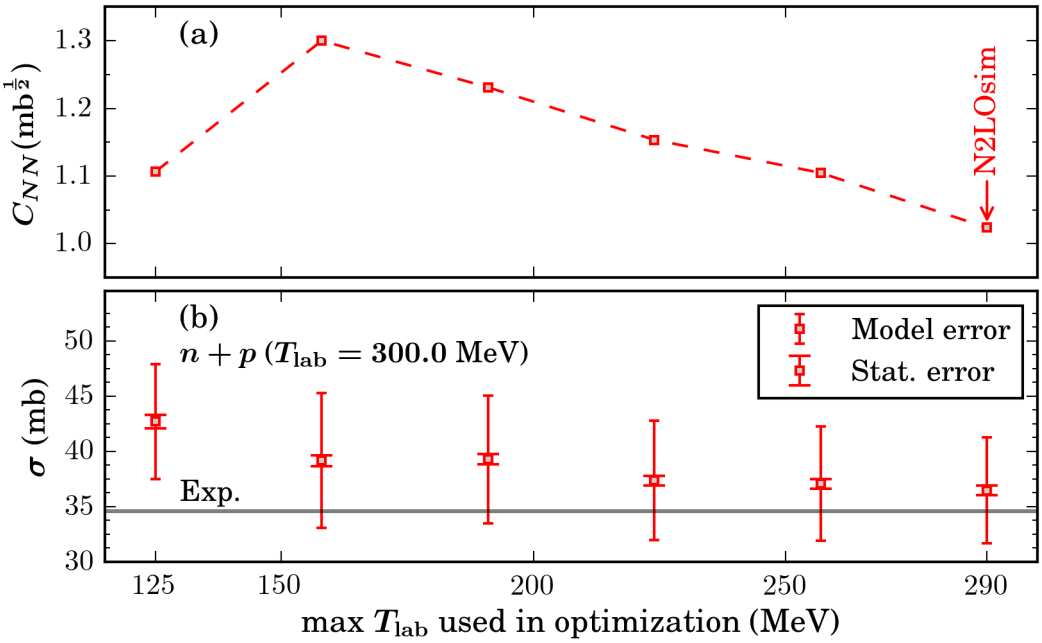

Figure 5.7: Results for the six potentials optimized at N2LO using different upper limits $T_{\rm lab}^{\rm max}$ for the NN scattering data included in the objective function. (a) The NN model scaling constant $C_{\rm NN}$. (b) The total cross section σ for np scattering at $T_{\rm lab}$ = 300 MeV. The gray band indicates the experimental value. (From Paper 2)

different for each potential. We used the limits 125, 158, 191, 224, 257 and 290 MeV for $T_{\rm lab}^{\rm max}$. Thus, the last potential is identical to NNLOsim.

In Fig. 5.7(a) we show the model error scaling constant $C_{\rm NN}$ that determines the size of the adopted model error. It is roughly the same for all of the different potentials.

Next we look at some predictions using these potentials. In Fig. 5.7(b) we show the prediction for the np total cross section, σ, at a scattering energy $T_{\rm lab}$ = 300 MeV. For this observable we can compare the variation with the previously approximated model error. The variation between predictions is of approximately the same size as the N2LOsim model error, while the statistical error is significantly smaller.

This suggests that the size of the model error can be well approximated using the range of variation. This enables us to estimate the model uncertainty in bound-state observables. In Fig. 5.8(a) we show our predictions for $E(^4\text{He})$ together with the experimental value. This estimation of the model

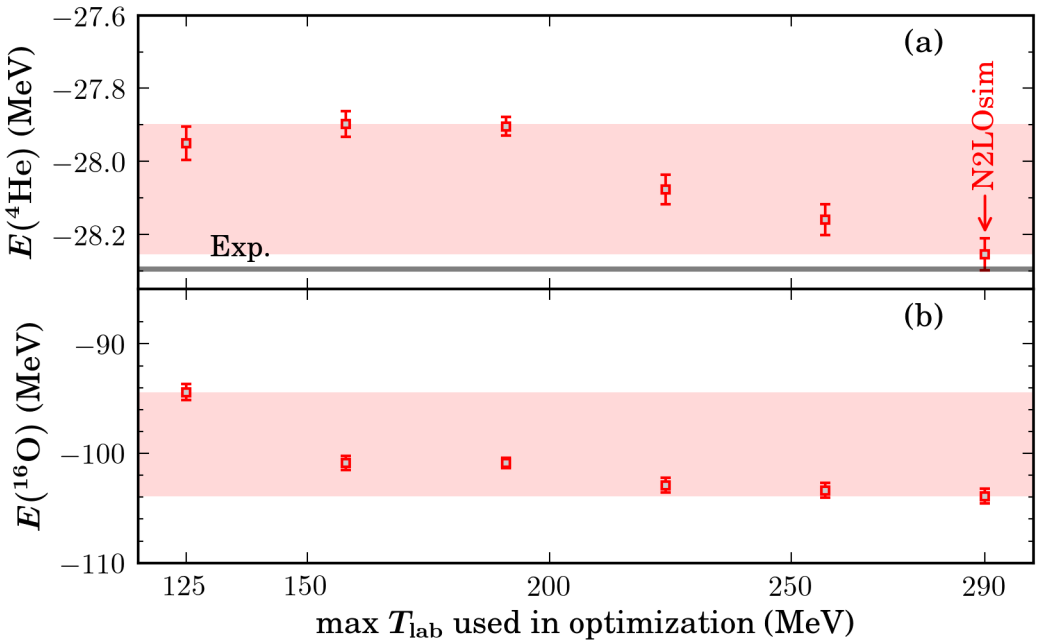

Figure 5.8: Results for the six potentials optimized at N2LO using different upper limits $T_{\mathrm{lab}}^{\mathrm{max}}$ for the NN scattering data included in the objective function. (a) The binding energy of ^{4}He. (b) The binding energy of ^{16}O. In both cases the statistical uncertainties are much smaller than the estimation of the model error, shown with a red band. (From Paper 2)

error suggests it is around 0.4 MeV, or 0.1 MeV/A. Just as for the scattering observables this is significantly larger than the statistical uncertainty.

Both the T_{lab} = 300 MeV NN scattering cross section and the ^{4}He binding energy are in some sense similar to data already included in the objective function. To see how well the N2LOsim potential performs for heavier systems, we computed the binding energy of ^{16}O, $E(^{16}\mathrm{O})$. These computations were performed using the coupled cluster (CC) method, using the so-called Λ-CCSD(T) approximation [62] with 15 major oscillator shells and $\hbar\omega$ = 22 MeV. For more details see Paper 2. To calculate the statistical uncertainties for $E(^{16}\mathrm{O})$ we performed a Monte Carlo sampling with N_{mc} = 2.5×10^4 samples for each of the six potentials. A Monte Carlo sampling was used since we have not implemented AD for the CC calculations. The sampling was done using the doubles approximation (CCSD) with 9 major oscillator shells.

Results for $E(^{16}\mathrm{O})$ are shown in Fig. 5.8(b). The statistical uncertainties are very small, a few hundred keV, compared to the variation between potentials. The model error from the variation is estimated to around 10 MeV or 0.6 MeV/A – considerably larger than for $E(^{4}\mathrm{He})$. The only difference between the six potentials is the amount of high-energy NN scattering data that is included. We still include the same πN data and bound-state properties as in the N2LOsim potential. This suggests that it is very difficult to make accurate predictions for heavier systems when only observables for $A \leq 3$ are included in the objective function.

Table 5.4: Theoretical values with statistical uncertainties propagated from the LECs. The observables shown are the ground-state energies (in MeV) and radii (in fm) for $A \leq 4$ nuclei and the $^1S_0$ ERE parameters (in fm). For the deuteron we also include the D-state probability $D(^2H)$ (in percent) and the quadrupole moment $Q(^2H)$ (in fm^2). Gray background indicates that the observable was not included in the objective function making it a prediction. The error bars on the experimental values for bound-state observables include both experimental and method uncertainties as detailed in Tab. 3.2. (From Paper 2)

	LOsim	NLOsim	N2LOsim	Experiment	Ref.
$E(^2\mathrm{H})$	−2.225	$-2.225^{(+1)}_{(-6)}$	$-2.225^{(+0)}_{(-1)}$	−2.225	Tab. 3.2
$E(^3\mathrm{H})$	−11.44	$-8.268^{(+27)}_{(-38)}$	$-8.482^{(+2)}_{(-5)}$	−8.482(3)	Tab. 3.2
$E(^3\mathrm{He})$	−10.44	$-7.528^{(+20)}_{(-31)}$	$-7.718^{(+2)}_{(-6)}$	−7.718(4)	Tab. 3.2
$E(^4\mathrm{He})$	−40.39(1)	$-27.44^{(+13)}_{(-15)}$	$-28.26^{(+4)}_{(-5)}$	−28.30(1)	Tab. 3.2
$r_{\text{pt-p}}(^2\mathrm{H})$	+1.911	$+1.972^{(+0)}_{(-2)}$	+1.966	+1.976(1)	Tab. 3.2
$r_{\text{pt-p}}(^3\mathrm{H})$	+1.292	$+1.614^{(+2)}_{(-3)}$	+1.581(1)	+1.587(41)	Tab. 3.2
$r_{\text{pt-p}}(^3\mathrm{He})$	+1.368	+1.791(3)	+1.760(1)	+1.766(13)	Tab. 3.2
$r_{\text{pt-p}}(^4\mathrm{He})$	+1.080	$+1.482^{(+3)}_{(-4)}$	+1.445(2)	+1.455(7)	Tab. 3.2
$E_A^1(^3\mathrm{H})$	–	–	+0.6848(11)	+0.6848(11)	Tab. 3.2
$D(^2\mathrm{H})$	+7.809	$+2.875^{(+85)}_{(-82)}$	$+3.380^{(+46)}_{(-45)}$	–	
$Q(^2\mathrm{H})$	+0.3029	$+0.2589^{(+17)}_{(-19)}$	+0.2623(8)	+0.270(11)	Tab. 3.2
a_{nn}^{N}	−26.04(8)	$-18.95^{(+38)}_{(-41)}$	−19.25(12)	−18.95(40)	[4]
a_{np}^{N}	−25.58(8)	$-23.60^{(+10)}_{(-13)}$	−23.84(11)	−23.71	[38]
a_{pp}^{C}	−7.579(6)	$-7.799^{(+1)}_{(-3)}$	−7.811(1)	−7.820(3)	[30]
r_{nn}^{N}	+1.697(1)	$+2.752^{(+7)}_{(-8)}$	+2.794(3)	+2.75(11)	[4]
r_{np}^{N}	+1.700(1)	+2.648(3)	+2.686(2)	+2.750(62)	[38]
r_{pp}^{C}	+1.812(1)	+2.704(3)	+2.758(2)	+2.790(14)	[30]

Chapter 6

Discussion and outlook

In Ch. 5 we demonstrated that we could produce chiral interactions with good precision and increasing accuracy as the chiral order increased. We have taken advantage of the qualities of χEFT mentioned in the introduction: We have to some extent estimated the model uncertainties with the help of the power counting and we have used both NN, πN and few-nucleon data to constrain the model. In order to achieve this we have addressed and solved several technical challenges:

- The development of a robust and efficient minimization methodology.
- The computation of precise derivatives using AD.
- Accurate calculation and propagation of statistical uncertainties.

The methods described here already open the way for many more and deeper studies of χEFT. There are, however, still many aspects that can be improved upon. In the following Section we will try to outline the most important improvements and future studies that should be made.

6.1 Further improvements

The part of the theory that is most incomplete is still the estimation of the model uncertainty. In this Thesis we have mentioned three different methods to probe model uncertainties:

- (E1) Direct error estimates on scattering amplitudes obtained from the χEFT truncation error. Presented in Sec. 2.4

- (E2) Dependence of the observable values on unphysical model parameters such as the regulator cutoff Λ, see Ref. [5] for more details.

- (E3) Variations in observable values when using slightly different objective functions to constrain the LECs. See Sec. 5.1.

None of these methods are complete and they only produce crude estimates of the model uncertainties. However, already from these estimates it is possible to get an idea of the size of the model error, see Figs. 5.5 and 5.7.

We can conclude that the resulting statistical uncertainties are much smaller than the model error up to and including N2LO. The two estimates of the model error investigated in this Thesis, (E1) and (E3), produce similar sizes for the model error. Furthermore, the model error seems to increase for heavier systems, see Fig. 5.8. Still, more well defined ways to extract the model error is needed. One method, which shows great promise, is the use of Bayesian tools, see Refs. [63, 64]. Also the statistical uncertainties should be improved upon. In Sec. 4.4 we mentioned that the extraction of statistical errors rested on the assumption of normally distributed residuals. As we discussed in Sec. 5.2 and showed in Fig. 5.2 this is not entirely true. Another method which might produce more accurate statistical errors in this case is Lagrange multiplier analysis [65].

Apart from the model error estimates, improvements to the methods would also increase the accuracy of the theory. As mentioned already in Sec. 3.3.3 we made a number of approximations in the calculation of NN scattering data regarding the inclusion of electro-magnetic effects that may need improvement. The only method with a non-negligible method uncertainty is the NCSM, which would need larger model spaces to decrease the error.

There are many ways in which it is possible to use the methods presented in this Thesis for χEFT-related studies. One obvious step forward is to extend the analysis done in Paper 2 to also include N3LO.

Many new insights could be gained by performing an extended statistical and correlation analysis of the model and the data. For example, sensitivity analyses can determine which observables are needed to better constrain different parts of the model, see Ref. [66] for more details. Global correlations between observables, such as the well-known Tjon-line, can be obtained by constructing several different potentials and studying correlations between the predictions. As already seen in Sec. 5.3.4, different potentials can be

constructed by varying the used objective function. Another method is to vary model parameters such as the regulator parameter Λ.

An interesting and important extension of the work presented in this Thesis would be to calculate other types of observables. This can further constrain, test or falsify the model. Examples of such data could be three-body scattering, more properties of medium-mass nuclei, and infinite nuclear matter properties. The effect of including some medium-mass bound-state energies and radii in the objective function has already been explored in Ref. [67]. This showed promising results for the more accurate description of the ground states and excited states of medium-mass nuclei and of symmetric nuclear matter. We also saw in this Thesis and in Paper 2 that when including only observables for three and fewer nuclei we get very large uncertainties in heavier systems.

The estimate of the model error from using different objective functions can be more thoroughly tested using a much larger set of potentials. This analysis should be done for the lower chiral orders, and also for N3LO, to get a more complete picture.

6.2 Conclusions

Although there is much that can still be done, the methods described here have made the simultaneous optimization of NN, πN and few-nucleon experimental data possible. This constitutes an important step forward in the development of χEFT as a state-of-the art model for low-energy nuclear physics.

With the continuous development of χEFT up to higher orders, more accurate error estimates, improved methods for few-nucleon systems, and increased computing power – the field will continue to prosper.

Bibliography

[1] S. Aoki, "Nucleon-nucleon interactions via Lattice QCD: Methodology," *The European Physical Journal A* **49** no. 7, (2013) .

[2] R. Machleidt, "High-precision, charge-dependent Bonn nucleon-nucleon potential," *Phys. Rev. C* **63** (Jan, 2001) 024001.

[3] R. N. Pérez, J. E. Amaro, and E. R. Arriola, "Coarse-grained potential analysis of neutron-proton and proton-proton scattering below the pion production threshold," *Phys. Rev. C* **88** (Dec, 2013) 064002.

[4] R. Machleidt and D. Entem, "Chiral effective field theory and nuclear forces," *Physics Reports* **503** no. 1, (2011) 1 – 75.

[5] E. Epelbaum, W. Glöckle, and U.-G. Meißner, "The two-nucleon system at next-to-next-to-next-to-leading order," *Nuclear Physics A* **747** no. 2–4, (2005) 362 – 424.

[6] S. Weinberg, "Phenomenological Lagrangians," *Physica A: Statistical Mechanics and its Applications* **96** no. 1–2, (1979) 327 – 340.

[7] E. Jenkins and A. V. Manohar, "Baryon chiral perturbation theory using a heavy fermion lagrangian," *Physics Letters B* **255** no. 4, (1991) 558 – 562.

[8] S. Weinberg, "Nuclear forces from chiral lagrangians," *Physics Letters B* **251** no. 2, (1990) 288 – 292.

[9] S. Weinberg, "Effective chiral lagrangians for nucleon-pion interactions and nuclear forces," *Nuclear Physics B* **363** no. 1, (1991) 3 – 18.

[10] E. Epelbaum, "Few-nucleon forces and systems in chiral effective field theory," *Progress in Particle and Nuclear Physics* **57** no. 2, (2006) 654 – 741.

[11] U. van Kolck, M. C. M. Rentmeester, J. L. Friar, T. Goldman, and J. J. de Swart, "Electromagnetic Corrections to the One-Pion-Exchange Potential," *Phys. Rev. Lett.* **80** (May, 1998) 4386–4389.

[12] **UCNA** Collaboration, J. Liu, M. Mendenhall, A. Holley, H. Back, T. Bowles, L. Broussard, R. Carr, S. Clayton *et al.*, "Determination of the Axial-Vector Weak Coupling Constant with Ultracold Neutrons," *Phys. Rev. Lett.* **105** (Oct, 2010) 181803.

[13] L. Durand, "Vacuum Polarization Effects in Proton-Proton Scattering," *Phys. Rev.* **108** (Dec, 1957) 1597–1610.

[14] V. G. J. Stoks and J. J. de Swart, "Magnetic moment interaction in nucleon-nucleon phase-shift analyses," *Phys. Rev. C* **42** (Oct, 1990) 1235–1248.

[15] E. Epelbaum, A. Nogga, W. Glöckle, H. Kamada, U.-G. Meißner, and H. Witała, "Three-nucleon forces from chiral effective field theory," *Phys. Rev. C* **66** (Dec, 2002) 064001.

[16] K. Hebeler, H. Krebs, E. Epelbaum, J. Golak, and R. Skibiński, "Efficient calculation of chiral three-nucleon forces up to N^{3}LO for *ab initio* studies," *Phys. Rev. C* **91** (Apr, 2015) 044001.

[17] N. Fettes, U.-G. Meißner, and S. Steininger, "Pion-nucleon scattering in chiral perturbation theory (I): Isospin-symmetric case," *Nuclear Physics A* **640** no. 2, (1998) 199 – 234.

[18] K. Wendt, B. Carlsson, and A. Ekström, "Uncertainty Quantification of the Pion-Nucleon Low-Energy Coupling Constants up to Fourth Order in Chiral Perturbation Theory," `arXiv:1410.0646 [nucl-th]`.

[19] P. J. Mohr, B. N. Taylor, and D. B. Newell, "CODATA recommended values of the fundamental physical constants: 2010*," *Rev. Mod. Phys.* **84** (Nov, 2012) 1527–1605.

[20] J. Beringer, J. F. Arguin, R. M. Barnett, K. Copic, O. Dahl, D. E. Groom, C. J. Lin, J. Lys *et al.*, "Review of Particle Physics*," *Phys. Rev. D* **86** (Jul, 2012) 010001.

[21] K. Erkelenz, R. Alzetta, and K. Holinde, "Momentum space calculations and helicity formalism in nuclear physics," *Nuclear Physics A* **176** no. 2, (1971) 413 – 432.

[22] W. Glöckle, *The Quantum Mechanical Few-Body Problem*. Springer Berlin Heidelberg, 1983.

[23] I. Charpentier and J. Utke, "Rapsodia: User manual," tech. rep., Argonne National Laboratory, 2014. latest version available online at `http://www.mcs.anl.gov/Rapsodia/userManual.pdf`.

[24] Bystricky, J., Lehar, F., and Winternitz, P., "Formalism of nucleon-nucleon elastic scattering experiments," *J. Phys. France* **39** no. 1, (1978) 1–32.

[25] La France, P. and Winternitz, P., "Scattering formalism for nonidentical spinor particles," *J. Phys. France* **41** no. 12, (1980) 1391–1417.

[26] H. P. Stapp, T. J. Ypsilantis, and N. Metropolis, "Phase-Shift Analysis of 310-Mev Proton-Proton Scattering Experiments," *Phys. Rev.* **105** (Jan, 1957) 302–310.

[27] M. I. Haftel and F. Tabakin, "Nuclear saturation and the smoothness of nucleon-nucleon potentials," *Nuclear Physics A* **158** no. 1, (1970) 1 – 42.

[28] V. G. J. Stoks, R. A. M. Klomp, M. C. M. Rentmeester, and J. J. de Swart, "Partial-wave analysis of all nucleon-nucleon scattering data below 350 MeV," *Phys. Rev. C* **48** (Aug, 1993) 792–815.

[29] F. Calogero, *Variable Phase Approach to Potential Scattering*. Academic Press, 1967.

[30] J. R. Bergervoet, P. C. van Campen, W. A. van der Sanden, and J. J. de Swart, "Phase shift analysis of 0-30 MeV pp scattering data," *Phys. Rev. C* **38** (Jul, 1988) 15–50.

[31] C. M. Vincent and S. C. Phatak, "Accurate momentum-space method for scattering by nuclear and Coulomb potentials," *Phys. Rev. C* **10** (Jul, 1974) 391–394.

[32] R. A. Arndt, I. I. Strakovsky, and R. L. Workman, *SAID, Scattering Analysis Interactive Dial-in computer facility, George Washington University (formerly Virginia Polytechnic Institute), solution SM99 (Summer 1999); for more information see, e.g., R. A. Arndt, I. I. Strakovsky, and R. L. Workman, Phys. Rev. C* **50***, 2731 (1994).*, 1999.

[33] J. R. Bergervoet, P. C. van Campen, R. A. M. Klomp, J.-L. de Kok, T. A. Rijken, V. G. J. Stoks, and J. J. de Swart, "Phase shift analysis of all proton-proton scattering data below T_{lab}=350 MeV," *Phys. Rev. C* **41** (Apr, 1990) 1435–1452.

[34] H. A. Bethe, "Theory of the Effective Range in Nuclear Scattering," *Phys. Rev.* **76** (Jul, 1949) 38–50.

[35] B. Gabioud, J. C. Alder, C. Joseph, J. F. Loude, N. Morel, A. Perrenoud, J. P. Perroud, M. T. Tran *et al.*, "$n-n$ Scattering Length from the Photon Spectra of the Reactions $\pi^- d \to \gamma$nn and $\pi^- p \to \gamma n$," *Phys. Rev. Lett.* **42** (Jun, 1979) 1508–1511.

[36] D. E. Gonzalez Trotter, F. S. Meneses, W. Tornow, C. R. Howell, Q. Chen, A. S. Crowell, C. D. Roper, R. L. Walter *et al.*, "Neutron-deuteron breakup experiment at E_n = 13 MeV: Determination of the $^1S_0$ neutron-neutron scattering length a_{nn}," *Phys. Rev. C* **73** (Mar, 2006) 034001.

[37] Q. Chen, C. R. Howell, T. S. Carman, W. R. Gibbs, B. F. Gibson, A. Hussein, M. R. Kiser, G. Mertens *et al.*, "Measurement of the neutron-neutron scattering length using the $\pi^- d$ capture reaction," *Phys. Rev. C* **77** (May, 2008) 054002.

[38] R. W. Hackenburg, "Neutron-proton effective range parameters and zero-energy shape dependence," *Phys. Rev. C* **73** (Apr, 2006) 044002.

[39] P. Navrátil, G. P. Kamuntavičius, and B. R. Barrett, "Few-nucleon systems in a translationally invariant harmonic oscillator basis," *Phys. Rev. C* **61** (Mar, 2000) 044001.

[40] E. Anderson, Z. Bai, C. Bischof, S. Blackford, J. Demmel, J. Dongarra, J. Du Croz, A. Greenbaum *et al.*, *LAPACK Users' Guide*. Society for Industrial and Applied Mathematics, Philadelphia, PA, third ed., 1999. http://www.netlib.org/lapack/lug.

[41] J. L. Friar, A. Gal, J. W. Negele, D. W. L. Sprung, and M. K. Srivastava, *Advances in Nuclear Physics*, vol. 8. Springer US, New York, 1975.

[42] I. Angeli and K. Marinova, "Table of experimental nuclear ground state charge radii: An update," *Atomic Data and Nuclear Data Tables* **99** no. 1, (2013) 69 – 95.

[43] U. D. Jentschura, "Proton radius, Darwin-Foldy term and radiative corrections," *The European Physical Journal D* **61** no. 1, (2011) 7–14.

[44] D. Gazit, S. Quaglioni, and P. Navrátil, "Three-Nucleon Low-Energy Constants from the Consistency of Interactions and Currents in Chiral Effective Field Theory," *Phys. Rev. Lett.* **103** (Sep, 2009) 102502.

[45] Y. Akulov and B. Mamyrin, "Half-life and value for the bare triton," *Physics Letters B* **610** no. 1–2, (2005) 45 – 49.

[46] A. Huber, T. Udem, B. Gross, J. Reichert, M. Kourogi, K. Pachucki, M. Weitz, and T. W. Hänsch, "Hydrogen-Deuterium $1S - 2S$ Isotope Shift and the Structure of the Deuteron," *Phys. Rev. Lett.* **80** (Jan, 1998) 468–471.

[47] M. Giles, "An extended collection of matrix derivative results for forward and reverse mode automatic differentiation," Tech. Rep. NA-08/01, Oxford University Computing Laboratory, January, 2008. http://www.cs.ox.ac.uk/files/723/NA-08-01.pdf. This is an extended version of a paper which will appear in the proceedings of AD2008, the 5th International Conference on Automatic Differentiation.

[48] R. L. Workman, R. A. Arndt, W. J. Briscoe, M. W. Paris, and I. I. Strakovsky, "Parameterization dependence of T-matrix poles and eigenphases from a fit to πN elastic scattering data," *Phys. Rev. C* **86** (Sep, 2012) 035202.

[49] H. Krebs, A. Gasparyan, and E. Epelbaum, "Chiral three-nucleon force at N^{4}LO: Longest-range contributions," *Phys. Rev. C* **85** (May, 2012) 054006.

[50] B. Tromborg, S. Waldenstrøm, and I. Øverbø, "Electromagnetic corrections in hadron scattering, with application to πN $\to$ πN," *Helv. Phys. Acta* **51** no. 4, (1978) 584.

[51] B. Tromborg and J. Hamilton, "Electromagnetic corrections to hadron-hadron scattering," *Nuclear Physics B* **76** no. 3, (1974) 483 – 540.

[52] B. Tromborg, S. Waldenstrøm, and I. Øverbø, "Electromagnetic corrections to πN scattering," *Phys. Rev. D* **15** (Feb, 1977) 725–729.

[53] D. Bugg, "Coulomb corrections to πN elastic scattering," *Nuclear Physics B* **58** no. 2, (1973) 397 – 407.

[54] T. Mehen, I. W. Stewart, and M. B. Wise, "Wigner Symmetry in the Limit of Large Scattering Lengths," *Phys. Rev. Lett.* **83** (Aug, 1999) 931–934.

[55] J. Dobaczewski, W. Nazarewicz, and P.-G. Reinhard, "Error estimates of theoretical models: a guide," *Journal of Physics G: Nuclear and Particle Physics* **41** no. 7, (2014) 074001. http://stacks.iop.org/0954-3899/41/i=7/a=074001.

[56] S. Wild, "Solving derivative-free nonlinear least squares with POUNDERS," *Preprint ANL/MCS-P5120-0414, Argonne Nat. Lab., Argonne, IL* (2014) . http://www.mcs.anl.gov/publication/solving-derivative-free-nonlinear-least-squares-pounders.

[57] M. Galassi, "GNU Scientific Library Reference Manual." Http://www.gnu.org/software/gsl, Dec, 2014. http://www.gnu.org/software/gsl.

[58] T. Munson, J. Sarich, S. Wild, S. Benson, and L. C. McInnes, "TAO 2.0 Users Manual," Tech. Rep. ANL/MCS-TM-322, Mathematics and Computer Science Division, Argonne National Laboratory, 2012. http://www.mcs.anl.gov/tao.

[59] W. H. Press, S. A. Teukolsky, W. T. Vetterling, and B. P. Flannery, *Numerical Recipes in C (2Nd Ed.): The Art of Scientific Computing*. Cambridge University Press, New York, NY, USA, 1992. http://apps.nrbook.com/c/index.html.

[60] S. Klarsfeld, J. Martorell, J. Oteo, M. Nishimura, and D. Sprung, "Determination of the deuteron mean square radius," *Nuclear Physics A* **456** no. 3, (1986) 373 – 396.

[61] J. L. Friar, J. Martorell, and D. W. L. Sprung, "Nuclear sizes and the isotope shift," *Phys. Rev. A* **56** (Dec, 1997) 4579–4586.

[62] G. Hagen, T. Papenbrock, M. Hjorth-Jensen, and D. J. Dean, "Coupled-cluster computations of atomic nuclei," *Reports on Progress in Physics* **77** no. 9, (2014) 096302.

[63] R. J. Furnstahl, D. R. Phillips, and S. Wesolowski, "A recipe for EFT uncertainty quantification in nuclear physics," *Journal of Physics G: Nuclear and Particle Physics* **42** no. 3, (2015) 034028.

[64] R. J. Furnstahl, N. Klco, D. R. Phillips, and S. Wesolowski, "Quantifying truncation errors in effective field theory," arXiv:1506.01343 [nucl-th].

[65] D. Stump, J. Pumplin, R. Brock, D. Casey, J. Huston, J. Kalk, H. L. Lai, and W. K. Tung, "Uncertainties of predictions from parton distribution functions. I. The Lagrange multiplier method," *Phys. Rev. D* **65** (Dec, 2001) 014012.

[66] M. Kortelainen, T. Lesinski, J. Moré, W. Nazarewicz, J. Sarich, N. Schunck, M. V. Stoitsov, and S. Wild, "Nuclear energy density optimization," *Phys. Rev. C* **82** (Aug, 2010) 024313.

[67] A. Ekström, G. R. Jansen, K. A. Wendt, G. Hagen, T. Papenbrock, B. D. Carlsson, C. Forssén, M. Hjorth-Jensen *et al.*, "Accurate nuclear radii and binding energies from a chiral interaction," *Phys. Rev. C* **91** (May, 2015) 051301.